Stellar configurations in $f(R, L_m, T)$ gravity: probing anisotropy and stability via minimal geometric deformation

M. Zubair[1,2†] Hira Sohail[3‡] Saira Waheed[4§] Amara Ilyas[5,6,7♮] Irfan Mahmood[3♯]

[1]Department of Mathematics, COMSATS University Islamabad, Lahore 54000, Pakistan
[2]National Astronomical Observatories, Chinese Academy of Sciences, Beijing 100101, China
[3]Centre for High Energy Physics, University of the Punjab, Lahore 54590 , Pakistan
[4]Prince Mohammad Bin Fahd University, Al Khobar 31952, Kingdom of Saudi Arabia
[5]Department of Astronomy, School of Physical Sciences, University of Science and Technology of China, Hefei 230026, China
[6]CAS Key Laboratory for Researches in Galaxies and Cosmology, University of Science and Technology of China, Hefei 230026, China
[7]School of Astronomy and Space Science, University of Science and Technology of China, Hefei 230026, China

Abstract: This study uses a minimal geometric deformation scheme within the $f(\mathcal{R},\mathcal{L}_m,T)$ gravity paradigm to model anisotropic compact stars using class-1 embedding spacetime. We introduce the deformation of the radial component of the metric tensor, which decouples the Einstein field equations and introduces an additional gravitational source. The relevant constants are evaluated using observational data from seven realistic star candidates by matching the inner region with the outer Schwarzschild line element. A comprehensive graphical analysis of three compact stars is performed to examine the impact of the coupling parameter β and deformation parameter n, revealing positive, well-behaved energy densities and pressures that satisfy the energy conditions. The study found that negative values of the coupling parameter β allow greater mass accumulation while preserving key physical characteristics, such as stability under Herrera's cracking condition and the extended Tolman-Oppenheimer-Volkoff equation. This study highlights the significance of gravitational decoupling for determining mass, redshift, and compactness and provides important insights into the internal structure of stellar bodies within this new generalized gravity framework.

Keywords: gravitational decoupling, $f(\mathcal{R},\mathcal{L}_m,T)$ gravity, minimal geometric deformation

DOI: 10.1088/1674-1137/ae1202 **CSTR:** 32044.14.ChinesePhysicsC.50025103

I. INTRODUCTION

In 1916, Albert Einstein introduced the theory of general relativity (GR), which revolutionized our current understanding of gravitational phenomena and explained various critical astronomical events, including the curvature of spacetime and the formation of stellar as well as galactic structures. One of the most significant predictions of GR is the existence of black holes and compact stellar configurations, all of which result from the gravitational collapse during the final stages of a star's life. In 2005, numerous compact objects with high densities were discovered [1]. The theory of GR has continued to demonstrate its accuracy, as evidenced by the precise prediction of gravitational waves by Mercury's perihelion precession, which are recently detected by the Laser Interferometer Gravitational-Wave Observatory in collaboration with Virgo [2]. Additionally, the first picture of the shadow of a black hole, captured by the Event Horizon Telescope project, further validated the theory of GR [3]. Despite these remarkable successes, GR has encountered challenges in addressing certain theoretical and observational cosmic issues, such as the unexpected acceleration of the cosmos [4−7], non−renormalizability [8], cosmological constant problem [9], and mysteries surrounding the dark terms of cosmic distributions [10].

Numerous extended gravitational frameworks have been proposed to address the limitations of GR. These theories serve as candidates for DE, which is often believed to be responsible for accelerated cosmic expansion owing to its negative pressure. Many of these theories involve geometric modifications of the GR, providing essential frameworks to support observational cosmic data. For example, $F(\mathcal{R})$ gravity modifies the gravitation-

Received 30 June 2025; Accepted 9 October 2025; Accepted manuscript online 10 October 2025
† E-mail: mzubairkk@gmail.com; drmzubair@cuilahore.edu.pk
‡ E-mail: hirasohail02@outlook.com
§ E-mail: swaheed@pmu.edu.sa
♮ E-mail: aarks@ustc.edu.cn
♯ E-mail: mahirfan@yahoo.com

al theory by introducing a Lagrangian that is a function of the Ricci scalar [11, 12]. Another significant theory is teleparallel gravity in which the curvature $\mathcal{R}$ is substituted by torsion $\mathcal{T}$ and is defined by the Weitzenböck connection instead of the Levi-Civita connection [13, 14]. Initially, this framework was applied to BTZ black hole solutions [15]. Subsequently, a study [16] revealed that $F(\mathcal{T})$ theory fails to comply with the first thermodynamical law of black holes. Examples of other remarkably modified theories of gravity include $f(R,R^{\alpha\beta}_{\alpha\beta},\Phi)$ [17−19], $f(G)$ gravity [20], $f(\mathcal{R},T)$ gravity [21], $f(\mathcal{T},B)$ gravity [22], $f(T,\mathcal{T})$ [23−26], $f(Q,T)$ [27, 28], and $f(\mathcal{R},\mathcal{L}_m)$ theory [29].

A particularly important class of modified theories involves coupling matter and geometry, such as $f(\mathcal{R},T)$ and $f(\mathcal{R},\mathcal{L}_m)$, and their unification in $f(\mathcal{R},\mathcal{L}_m,T)$ gravity. These frameworks allow the energy-momentum tensor to directly influence spacetime geometry, leading to richer phenomenology and the emergence of non-conserved matter fields. Recent studies have applied such theories to model anisotropic compact stars, explore deviations in hydrostatic equilibrium, and test the energy conditions under strong gravity. Additionally, the Minimal Geometric Deformation (MGD) technique has been increasingly utilized to generate exact or semi-analytical anisotropic solutions within these extended frameworks, demonstrating compatibility with astrophysical observations. Collectively, these advancements indicate that modified gravity continues to be a fertile ground for addressing outstanding questions in theoretical and observational cosmology. This theory considers the gravitational Lagrangian as a generic function of three fundamental quantities: the Ricci scalar $\mathcal{R}$, matter Lagrangian $\mathcal{L}_m$, and trace of the energy-momentum tensor T, that is, $\mathcal{L}_{\rm grav} = f(\mathcal{R},\mathcal{L}_m,T)$ [30−32]. Recent developments have shown that such frameworks can accommodate more realistic compact star models, account for anisotropic matter distributions, and generate modified equilibrium conditions that are consistent with astrophysical observations. Motivated by these advances, the present study explores anisotropic compact stellar configurations within the $f(\mathcal{R},\mathcal{L}_m,T)$ gravity framework using the MGD technique under the gravitational decoupling approach. This allows us to construct physically viable solutions while incorporating non-minimal matter-geometry coupling that reflects the current direction of research in gravitational modeling.

In recent years, the quest for exact spherically symmetric solutions to the dynamical field equations has become increasingly challenging, primarily because of the presence of numerous non-linear terms, especially in the context of modified gravity theories. A substantial body of literature is available wherein compact star solutions have been constructed using various gravitational frameworks. Nashed and El Hanafy [33] investigated spherically symmetric dynamical configurations in $f(\mathcal{R})$ gravity using a quadratic model defined by $f(\mathcal{R}) = \mathcal{R} + \epsilon\mathcal{R}^2$. For the interior spacetime geometry, they adopted the Krori-Barua metric and considered anisotropic matter distributions. Utilizing the observational data of PSR $J0740+6620$ from NICER and XMM-Newton observations, they determined the viable values of the parameter ϵ and demonstrated that the resulting structure is stable and satisfies all essential physical conditions. Extending this study, Nashed and Capozziello [34] employed an exponential model, $f(\mathcal{R}) = \mathcal{R}e^{\zeta\mathcal{R}}$, in combination with observational data from pulsar SAX J1748.9–2021, yielding significant results. In another investigation, Nashed [35] obtained exact solutions for anisotropic, perfect-fluid spheres within the $f(\mathcal{R},T)$ framework, adopting a linear form of the function as $f(\mathcal{R},T) = \mathcal{R} + \beta T$, where β is a dimensional parameter. The resulting solutions were in hydrostatic equilibrium, with all relevant physical quantities expressed in terms of β and compactness parameter $C = \dfrac{2GM}{\mathcal{R}c^2}$. Within the same theoretical context, the author further derived solutions by introducing specific assumptions on anisotropy and radial metric components, leading to compelling physical conclusions.

In the framework of conformal $f(\mathcal{R},T)$ gravity, Das et al. [36] explored the modeling of compact stars, where solutions were generated to describe the interior geometry of compact objects using a barotropic equation of state (EoS). A detailed graphical analysis demonstrated that the obtained solutions were physically consistent and corresponded to radiating compact stars. Kumar et al. [37] constructed stellar models with isotropic matter distributions in curvature-matter coupled gravity, assuming a linear functional form of $f(\mathcal{R},T)$. Their analysis confirmed the stability of the proposed configuration through various physical criteria. The pursuit of anisotropic and non-singular compact star models was further conducted in [38], where the barotropic EoS was applied within the $f(\mathcal{R},T)$ framework. The results indicated that the energy conditions were satisfied and the models exhibited a stable behavior. In another recent study [39], compact stellar configurations were investigated by employing the Krori-Barua metric as the interior geometry within the context of $\kappa(\mathcal{R},T)$ gravity. Utilizing observational data from three compact stars—4U 1820–30, SAX J1808.4–3658, and Her X–1—the physical acceptability and stability of the models were examined using graphical methods.

The gravitational decoupling technique, using MGD, offers a novel strategy that facilitates the derivation of acceptable solutions for spherically relativistic configurations. This method introduces various new elements that contribute to the pursuit of solutions for spherically symmetric objects by incorporating more complex gravitational sources into the existing energy-momentum tensor

while preserving spherical symmetry. The MGD approach was first presented by Ovalle within the framework of the Randall-Sundrum brane-world scenario [40, 41]. It was later extended to deform the standard Schwarzschild solution [42], leading to the formulation of new black hole models [43]. Initial applications of this technique were primarily developed in the context of brane-world models [44, 45], black hole acoustics [46], and studies on the Generalized Uncertainty Principle (GUP) and Hawking radiation involving fermions [47]. Additionally, it was applied to purely anisotropic matter distributions [48, 49] and the anisotropic Einstein-Maxwell system [50, 51]. Subsequently, this technique has been employed in various theories, such as in [52], where the MGD approach was used to extend the Buchdahl solution, and in [53], where it was applied to obtain an anisotropic static BTZ model in a $(2+1)$-dimensional spacetime. Other applications can also be found in the literature [54−56]. In particular, within the context of $f(\mathcal{R},T)$ theory, references are provided in [57, 58]. In the context of $F(R,T)$ theory, researchers [59] modeled new anisotropic compact stars based on the decoupling approach. To achieve this target, they assumed a linear selection of the $F(R,T)$ function—a well-known ansatz for metric potential, namely the modified Durgapal-Fuloria model and Pseudo-Isothermal dark matter—as a new source for the anisotropic seed solution. The obtained solution was nonsingular and agreed with all necessary physical conditions. In the context of GR, a previous study [60] adopted the decoupling method to focus on the strange star model and argued that through mass-radius analysis conducted for neutron star mergers and huge pulsars, the model parameters can be effectively constrained. It was concluded that their outcomes exceeded the observed masses of compact stars and also showed a correlation of recent findings from gravitational wave events, such as GW190814 and GW200210.

Following the work of Nashed *et al.* [33−35], the primary target of this study is to utilize the radii and masses of some known pulsars located within globular clusters and constrain different model parameters. By performing graphical analysis, we will assess whether the proposed MGD-based model in the realm of $f(R,L_m,T)$ gravity remains physically valid for the observed compact star candidates with known radii and masses. Therefore, we will select well-known stars and test our model against their properties. Specifically, we shall perform a complete physical analysis (including energy conditions and stability) for one representative star. For other known stars, we shall include the relevant numerical results in tabular form to show the variation in the values of different parameters (c,B,A) under different configurations, which can further change the behavior of all physical properties. This dual approach can allow us to validate the model across multiple realistic scenarios.

In this work, we shall construct anisotropic compact star models within the framework of $f(\mathcal{R},\mathcal{L}_m,T)$ gravity using the gravitational decoupling approach via MGD and embedding class-I spacetime. By deforming the radial metric component, the field equations will be decoupled into isotropic and anisotropic sectors, enabling the construction of physically viable models that are consistent with the observed stellar data. This work aims to explore the influence of the generalized theory, which unifies previous models such as $f(\mathcal{R},T)$ and $f(\mathcal{R},\mathcal{L}_m)$, on the key physical features of compact stars such as stability, energy conditions, and mass-radius behavior. The manuscript is organized as follows: Section II outlines the theoretical framework of this modified gravity, Section III discusses the metric and matching conditions, Section IV presents a detailed physical analysis, and Section V concludes our main findings.

II. BASICS OF $f(\mathcal{R},\mathcal{L}_m,T)$ THEORY

Because our primary objective is to study compact star models beyond the paradigm of GR, specifically within the framework of $f(\mathcal{R},\mathcal{L}_m,T)$ theory, this section provides an overview of the primary mathematical structure of this modified gravity theory, along with the necessary assumptions required to achieve the outlined goal. Haghani and Harko [30] proposed a novel framework that unifies the $f(\mathcal{R},T)$ and $f(\mathcal{R},\mathcal{L}_m)$ theories. This innovative approach leads to a new Lagrangian density incorporating the Ricci scalar, trace of the energy-momentum tensor, and Lagrangian of ordinary matter, defined by the following gravitational action:

$$S=\frac{1}{16\pi}\int f(\mathcal{R},\mathcal{L}_m,T)\sqrt{-g}\,\mathrm{d}^4x+\int\mathcal{L}_m\sqrt{-g}\,\mathrm{d}^4x +\beta\int\mathcal{L}_\vartheta\sqrt{-g}\,\mathrm{d}^4x. \tag{1}$$

Here, $f(\mathcal{R},\mathcal{L}_m,T)$ is a generic function of geometrical and gravitational quantities, and thus leads to the violation of the principle of minimal interaction between matter and geometry [30]. Consequently, unlike GR, the dynamical equations can no longer be written in the conventional form where *spacetime geometry equals ordinary matter*, hence, the standard conservation of the energy-momentum tensor is not guaranteed. Furthermore, the quantities $\mathcal{L}_m$ and $\mathcal{L}_\vartheta$ correspond to the matter and additional gravitational source sectors (commonly referred to as the ϑ–sector), respectively. A dimensionless constant β, representing the coupling parameter, is introduced. In metric formalism, the variation in the action with respect to $g^{\mu\nu}$ yields the following field equations:

$$f_{\mathcal{R}}\mathcal{R}_{\mu\nu}-\frac{1}{2}[f-(f_{\mathcal{L}}+2f_T)\mathcal{L}_m]g_{\mu\nu}+(g_{\mu\nu}\Box-\nabla_\mu\nabla_\nu)f_{\mathcal{R}}$$
$$=\left[8\pi G+\frac{1}{2}(f_{\mathcal{L}}+2f_T)\right]T_{\mu\nu}+8\pi G\beta\vartheta_{\mu\nu}+f_T\tau_{\mu\nu}, \tag{2}$$

where $f_{\mathcal{R}}=\partial f/\partial\mathcal{R}$, $f_T=\partial f/\partial T$, $f_{\mathcal{L}}=\partial f/\partial\mathcal{L}$ and $\Box=g^{\mu\nu}\nabla_\mu\nabla_\nu$. Here, the covariant derivative is symbolized by ∇_ν. Further, the $T_{\mu\nu}$, extra source $\vartheta_{\mu\nu}$, and $\tau_{\mu\nu}$ terms are, respectively, given as

$$T_{\mu\nu}=g_{\mu\nu}\mathcal{L}_m-2\partial\mathcal{L}_m/\partial g^{\mu\nu}, \tag{3}$$

$$\vartheta_{\mu\nu}=g_{\mu\nu}\mathcal{L}_\vartheta-2\partial\mathcal{L}_\vartheta/\partial g^{\mu\nu}, \tag{4}$$

$$\tau_{\mu\nu}=g^{\alpha\beta}\delta T_{\alpha\beta}/\delta g^{\mu\nu}. \tag{5}$$

Eq. (2) can be re-arranged as follows:

$$G_{\mu\nu}=\frac{1}{f_{\mathcal{R}}}\left[(8\pi G+(f_T+\frac{1}{2}f_{\mathcal{L}}))T_{\mu\nu}+\frac{1}{2}(f-\mathcal{R}f_{\mathcal{R}})g_{\mu\nu}\right.$$
$$\left.-(f_T+\frac{1}{2}f_{\mathcal{L}})\mathcal{L}_m g_{\mu\nu}+(\nabla_\mu\nabla_\nu-g_{\mu\nu}\Box)f_{\mathcal{R}}+f_T\tau_{\mu\nu}\right]. \tag{6}$$

In this setup, we assume the spherically symmetric metric written in following form:

$$\mathrm{d}s^2=-\mathrm{e}^{\nu(r)}\mathrm{d}t^2+\mathrm{e}^{\xi(r)}\mathrm{d}r^2+r^2\left(\mathrm{d}\theta^2+\sin^2\theta\mathrm{d}\phi^2\right). \tag{7}$$

The distribution of stellar matter is assumed to be an anisotropic fluid, which is defined by the following equation:

$$T_{\mu\nu}=(\rho+p_t)V_\mu V_\nu+p_t g_{\mu\nu}+(p_r-p_t)\chi_\mu\chi_\nu, \tag{8}$$

where ρ is energy density, and p_r and p_t denote the radial and transverse stresses, respectively. The four velocity, denoted by V_α and χ_α for the radial four vector, satisfies

$$V^u=\mathrm{e}^{\frac{-\nu}{2}}\delta^u_0,\quad V^uV_u=1,\quad \chi^u=\mathrm{e}^{\frac{-a}{2}}\delta^u_1,\quad \chi^u\chi_u=-1.$$

For the sake of simplicity in Eq. (6), we shall assume the well-motivated forms of Lagrangian matter $\mathcal{L}_m$ and $f(\mathcal{R},\mathcal{L}_m,T)$ function. In this study, we assume the Lagrangian matter form as $\mathcal{L}_m=(p_r+2p_t)/3$. Additionally, we assume a simple form of the $f(\mathcal{R},\mathcal{L}_m,T)$ function, which is given by

$$f(\mathcal{R},\mathcal{L}_m,T)=\mathcal{R}+\gamma T+\lambda\mathcal{L}_m, \tag{9}$$

where γ and λ are the coupling constants. The primary reason for selecting this model (9) is that it results in minimal coupling between matter and geometry, avoiding the complications of high order derivatives and enabling the successful implementation of either the MGD or e-MGD scheme. Earlier research has also employed similar functional forms to produce regular and physically feasible stellar models, such as in $f(R,T)$ [61] and $f(R,L_m)$ gravity [62]. Although there are fewer examples of studies on $f(R,L_m,T)$ gravity, where it was demonstrated to preserve central regularity and enable a physically consistent anisotropic extension, our work expands on this strategy and demonstrates that it is still efficient and consistent in this larger context. Interestingly, because model (9) is linear for all variables, that is, $\mathcal{R}$, $\mathcal{L}_m$ and T, the right hand side of Eq. (6) is similar to that obtained in GR theory as $f_{\mathcal{R}}=1$. In contrast, on the left hand side, quantities $\mathcal{L}_m$ and T alter the anisotropic fluid distribution via dimension-less interaction constants. Introducing this form of $f(\mathcal{R},\mathcal{L}_m,T)$ into Eq. (6), the following generic expression is obtained:

$$G_{\mu\nu}=8\pi GT_{\mu\nu}+8\pi G\beta\vartheta_{\mu\nu}+\left(\gamma+\frac{\lambda}{2}\right)T_{\mu\nu}$$
$$+\frac{1}{2}(\gamma T+\lambda\mathcal{L}_m)g_{\mu\nu}-\left(\gamma+\frac{\lambda}{2}\right)\mathcal{L}_m g_{\mu\nu}. \tag{10}$$

III. MGD AND EMBEDDING CLASS-I SPACE TIME

In this section, we introduce the concept of minimal geometric deformation, which introduces anisotropy into the set of field equations. This method incorporates an additional gravitational source, $\vartheta_{\mu\nu}$, into the energy-momentum tensor through gravitational decoupling. The following transformation is introduced:

$$\mathrm{e}^{\nu(r)}\longrightarrow\mathrm{e}^{H(r)}+\beta\quad\eta(r), \tag{11}$$

$$\mathrm{e}^{-\xi(r)}\longrightarrow\mathrm{e}^{-W(r)}+\beta\quad\psi(r). \tag{12}$$

Here, the notations $\eta(r)$ and $\psi(r)$ denote the deformation functions introduced for the temporal and radial components of the spacetime metric, respectively. According to the MGD approach, one of these functions can be set to zero, that is, either $\eta(r)=0$ or $\psi(r)=0$. In this study, we $\eta(r)=0$, thereby introducing deformation exclusively in the radial component. The constant β serves as a free coupling parameter, and by setting $\beta=0$, the original field equations of $f(\mathcal{R},\mathcal{L}_m,T)$ gravity are recovered. Based on this framework, the resulting deformed function is expressed as follows:

$$e^{-\xi(r)} \longrightarrow e^{-W(r)} + \beta\psi(r). \tag{13}$$

We introduce the additional gravitational source $\vartheta_{\mu\nu}$ into the original energy-momentum tensor, resulting in the effective energy-momentum tensor for $f(\mathcal{R}, \mathcal{L}_m, T)$ gravity. The standard dynamical equations, expressed in terms of the MGD, can then be written as

$$\mathcal{R}_{\mu\nu} - \frac{1}{2}\mathcal{R}g_{\mu\nu} = 8\pi G T^{\text{eff}}_{\mu\nu}, \tag{14}$$

where

$$T^{\text{eff}}_{\mu\nu} = 8\pi G\hat{T}_{\mu\nu} + 8\pi G\beta\vartheta_{\mu\nu} = 8\pi G T_{\mu\nu} + \left(\gamma + \frac{\lambda}{2}\right) T_{\mu\nu} + \frac{1}{2}(\gamma T + \lambda\mathcal{L}_m) g_{\mu\nu} - \left(\gamma + \frac{\lambda}{2}\right)\mathcal{L}_m g_{\mu\nu} + 8\pi G\beta\vartheta_{\mu\nu}. \tag{15}$$

Here, the original energy-momentum tensor is given by $T_{\mu\nu} = \text{diag}(\rho, -p_r, -p_t, -p_t)$, whereas the additional gravitational source is represented as $\vartheta_{\mu\nu} = \text{diag}(\vartheta^0_0, \vartheta^1_1, \vartheta^2_2, \vartheta^3_3)$. The components of $\vartheta_{\mu\nu}$ introduce anisotropies into the self-gravitating system, thereby transforming the field equations into a set of quasi-Einstein field equations. This transformation is achieved through the deformation of the metric, and the resulting expressions for the effective energy density and pressures under gravitational decoupling are obtained as follows:

$$\rho^{\text{eff}} = \hat{\rho} + \beta\vartheta^0_0, \quad p^{\text{eff}}_r = \hat{p}_r - \beta\vartheta^1_1, \quad p^{\text{eff}}_t = \hat{p}_t - \beta\vartheta^2_2, \tag{16}$$

with

$$\hat{\rho} = 8\pi G\rho + \frac{1}{2}(3\gamma + \lambda)\rho - \frac{\gamma}{6}p_r - \frac{\gamma}{3}p_t, \tag{17}$$

$$\hat{p}_r = 8\pi G p_r - \frac{\gamma}{2}\rho + \left(\frac{7\gamma}{6} + \frac{\lambda}{2}\right) p_r + \frac{\gamma}{3}p_t, \tag{18}$$

$$\hat{p}_t = 8\pi G p_t - \frac{\gamma}{2}\rho + \frac{\gamma}{6}p_r + \left(\frac{4\gamma}{3} + \frac{\lambda}{2}\right) p_t. \tag{19}$$

The anisotropy parameter is defined as

$$\Delta = \frac{r}{2}(p^{\text{eff}}_t - p^{\text{eff}}_r) = \Delta + \Delta_\vartheta. \tag{20}$$

These relations effectively decouple the original dynamical equations into two distinct systems: one governing the seed isotropic matter distribution and the other characterizing the new anisotropic configuration arising from gravitational decoupling. By substituting Eq. (13) into the field Eqs. (17)–(19), two separate sets of equations can be obtained, where $\Delta = \frac{r}{2}(p_t - p_r)$ and $\Delta_\vartheta = \frac{r}{2}\beta(\vartheta^1_1 - \vartheta^2_2)$. The first system corresponds to the standard field equations governed by the energy-momentum tensor $T_{\mu\nu}$ in the limit $\beta = 0$, and is supplemented by a conservation equation. The governing equations are as follows:

$$\rho = \left(e^{-a(r)}\left(ra'(r)(16\gamma + 96\pi G + 6\lambda - \gamma r v'(r)) + 2\left(e^{a(r)} - 1\right)(8\gamma + 48\pi G + 3\lambda) + 2\gamma r^2 v''(r) + \gamma r^2 v'(r)^2 + 4\gamma r v'(r)\right)\right) \Big/ \left(3r^2(2\gamma + 16\pi G + \lambda)(4\gamma + 16\pi G + \lambda)\right), \tag{21}$$

$$p_r = \left(e^{-a(r)}\left(\gamma r a'(r)(r v'(r) + 8) - 2\left(\left(e^{a(r)} - 1\right)(8\gamma + 48\pi G + 3\lambda) + \gamma r^2 v''(r)\right) + 2r(10\gamma + 48\pi G + 3\lambda)v'(r) + \gamma\left(-r^2\right)v'(r)^2\right)\right) \Big/ \left(3r^2(2\gamma + 16\pi G + \lambda)(4\gamma + 16\pi G + \lambda)\right), \tag{22}$$

$$p_t = \left(e^{-a(r)}\left(-ra'(r)(8\gamma + r(10\gamma + 48\pi G + 3\lambda)v'(r) + 96\pi G + 6\lambda) + 2\gamma\left(8e^{a(r)} + 5r^2\left(2v''(r) + v'(r)^2\right) + 8rv'(r) - 8\right) + 3r(16\pi G + \lambda)\left(2rv''(r) + rv'(r)^2 + 2v'(r)\right)\right)\right) \Big/ \left(6r^2(2\gamma + 16\pi G + \lambda)(4\gamma + 16\pi G + \lambda)\right), \tag{23}$$

and the conservation equation is given by

$$-\frac{\mathrm{d}p_r}{\mathrm{d}r}-\frac{H(r)'}{2}(\rho+p_r)+\frac{2(p_t-p_r)}{r}+\frac{\mathrm{d}}{\mathrm{d}r}\left[\frac{\gamma}{6(8\pi G+\gamma+\lambda/2)}\left(3\rho-p_r-2p_t\right)\right]=0. \tag{24}$$

The spacetime solution for the aforementioned set of equations can be expressed by the following metric:

$$\mathrm{d}s^2=\mathrm{e}^{H(r)}\mathrm{d}t^2-\mathrm{e}^{W(r)}\mathrm{d}r^2-r^2(\mathrm{d}\theta^2+\sin^2\theta\mathrm{d}\varphi^2). \tag{25}$$

The quasi-Einstein equations are the second set of equations that apply to source $\vartheta_{\mu\nu}$. These are derived by using the relationships defined in Eq. (16) and the deformed metric supplied in Eq. (13), where $\beta\neq 0$. The resulting quasi-Einstein equations, along with the conservation equation, are as follows:

$$\vartheta_0^0=\Big(r\psi'(r)(\gamma rH'(r)-2(8\gamma+48\pi G+3\lambda))+\psi(r)\big(\gamma r(2rH''(r)+H'(r)(rH'(r)+4))-2(8\gamma+48\pi G+3\lambda)\big)\Big)\Big/\Big(3r^2(2\gamma+16\pi G+\lambda)(4\gamma+16\pi G+\lambda)\Big), \tag{26}$$

$$\vartheta_1^1=\Big(\gamma r(rH'(r)+8)\psi'(r)-\psi(r)\big(16\gamma+r(H'(r)(20\gamma+96\pi G-\gamma rH'(r)+6\lambda)-2\gamma rH''(r))+96\pi G+6\lambda\big)\Big)\Big/\Big(3r^2(2\gamma+16\pi G+\lambda)(4\gamma+16\pi G+\lambda)\Big), \tag{27}$$

$$\vartheta_2^2=-\Big(r\psi'(r)(8\gamma+r(10\gamma+48\pi G+3\lambda)H'(r)+96\pi G+6\lambda)+\psi(r)\big(r\big(2r(10\gamma+48\pi G+3\lambda)H''(r)+H'(r)(16\gamma+r(10\gamma+48\pi G+3\lambda)H'(r)+96\pi G+6\lambda)\big)-16\gamma\big)\Big)\Big/\Big(6r^2(2\gamma+16\pi G+\lambda)(4\gamma+16\pi G+\lambda)\Big), \tag{28}$$

$$-\frac{H(r)'}{2}(\vartheta_0^0-\vartheta_1^1)-\frac{\mathrm{d}\vartheta_1^1}{\mathrm{d}r}+\frac{2}{r}(\vartheta_2^2-\vartheta_1^1)+\frac{\mathrm{d}}{\mathrm{d}r}\left[\frac{\gamma}{6(8\pi G+\gamma+\lambda/2)}\left(3\vartheta_0^0+\vartheta_1^1+2\vartheta_2^2\right)\right]=0. \tag{29}$$

At this juncture, it is pertinent to note that the two sets of equations are decoupled, exhibit no exchange of energy between them, and interact solely through gravitational effects.

A. Class-I solutions and minimal geometric deformation scheme

To solve the two sets of field equations involving unknown functions $W(r)$ and $H(r)$, we select a metric potential that meets the key criteria: it must be finite, monotonically increasing with r, and reach a minimum at $r=0$, ensuring regularity. As outlined in [63], these conditions are essential for deriving physically viable static spherically symmetric perfect fluid solutions. In this study, we adopt the following form for the metric potential, which satisfies the necessary mathematical conditions and facilitates the derivation of physically viable expressions for the effective energy density and pressure. The chosen metric potential is given by

$$\mathrm{e}^W=1+cr^2\mathrm{e}^{nar^2}, \tag{30}$$

where c, n, and a are arbitrary constants. This specific form has been widely utilized as an ansatz, particularly in the construction of class-I solutions [64, 65]. Notably, this metric is consistent with the criterion of being regular at the center, exhibiting a monotonically increasing trend with a minimum at $r=0$ and $\mathrm{e}^W=1+O(r^2)$. Therefore, it is feasible to model compact stars using this theory. For a spacetime to be categorized under embedding class-I, it is imperative that Eq. (25) satisfies the Karmarkar condition, originally formulated by Karmarkar in 1948 [66]. This condition is expressed as follows:

$$\mathcal{R}_{1414} = \frac{\mathcal{R}_{1212}\mathcal{R}_{3434} + \mathcal{R}_{1224}\mathcal{R}_{1334}}{\mathcal{R}_{2323}}. \tag{31}$$

By incorporating the conditions specified in Eq. (31), and given that $R_{2323} \neq 0$, as noted in [67], we derive the following equation that establishes a relationship between the two spacetime functions, $W(r)$ and $H(r)$, as outlined below:

$$\frac{W'H'}{1-\mathrm{e}^{W}} = W'H' - 2H'' - H'^2, \tag{32}$$

where $\mathrm{e}^{W(r)} \neq 1$. By integrating the first equation, we derive the following equation, which illustrates the manner in which the four-dimensional spacetime, as described by Eq. (31), is embedded within a five-dimensional pseudo-Euclidean space. This corresponds to the solutions for embedding class-I. It is defined as

$$\mathrm{e}^{H(r)} = \left(\mathbb{A} + \mathbb{B}\int \sqrt{\mathrm{e}^{W(r)} - 1}\,\mathrm{d}r\right)^2, \tag{33}$$

where $\mathbb{A}$ and $\mathbb{B}$ are constants due to integration. Substituting Eq. (30) into the above equation allows us to determine the value of the metric $\mathrm{e}^{H(r)}$, as follows:

$$\mathrm{e}^{H(r)} = \left(\mathbb{A} + \frac{\mathbb{B}\sqrt{cr^2\mathrm{e}^{anr^2}}}{anr}\right)^2. \tag{34}$$

Constants $\mathbb{A}$, $\mathbb{B}$, and c can be evaluated by applying the matching condition. In the subsequent section, we fixed constants λ and a. Notably, the metric potential $\mathrm{e}^{H(r)}$ is a radial dependent monotonically increasing function and exhibits a positive, finite, and regular trend with $\mathrm{e}^{H(r)} \to 1$ as $r \to 0$, thus ensuring the absence of singularities. Therefore, this metric potential is suitable for modeling a relativistic compact object within the framework of $f(\mathcal{R}, T, \mathcal{L}_m)$ gravity using the MGD approach. The below-line element can be used to describe the field equations given by Eqs. (21) to (23):

$$\begin{aligned}\mathrm{d}s^2 = &-\left(\mathbb{A} + \frac{\mathbb{B}\sqrt{cr^2\mathrm{e}^{anr^2}}}{anr}\right)^2\mathrm{d}t^2 + \left(1 + cr^2\mathrm{e}^{nar^2}\right)^{-1}\mathrm{d}r^2 \\ &+ r^2\left(\mathrm{d}\theta^2 + \sin^2\theta\mathrm{d}\phi^2\right).\end{aligned} \tag{35}$$

To obtain the complete solutions for our model, the components of $\vartheta_{\mu\nu}$ must be calculated. This requires the determination of the deformation function $\psi(r)$. Several methods can be employed to determine $\psi(r)$, including

- mimicking the density constraint ($\vartheta_0^0 = \rho$);
- mimicking the pressure constraint ($\vartheta_1^1 = p_r$); and
- relating the components of $\vartheta_{\mu\nu}$ through various equations of state, such as polytropic, barotropic, or linear equations.

However, the determination of the deformation function, $\psi(r)$, often becomes mathematically intricate, particularly when aiming to maintain physical acceptability and analytical solvability. Therefore, we adopt a deformation function that is free from singularities, exhibits non-decreasing behavior, and has been extensively utilized in previous studies for constructing physically viable anisotropic models [52, 65, 68]. The selected form is not arbitrary; it is carefully selected to be fully compatible with the prescribed seed solution, thereby ensuring that the resulting field equations remain analytically tractable and physically consistent. Although alternative functional forms for $\psi(r)$ are theoretically permissible, they frequently introduce significant non-linearities or yield unphysical features, such as singularities or negative pressures. Moreover, the selected function has also been successfully employed in conjunction with the same seed metric in earlier studies, further justifying its use in the present analysis. This form is given by

$$\psi(r) = \frac{ncr^2}{cr^2 + 1}. \tag{36}$$

The complete spacetime structure related to the energy-momentum tensor $T_{\mu\nu}^{\mathrm{eff}}$ can be explicitly defined as follows:

$$\begin{aligned}\mathrm{d}s^2 = &-\left(\mathbb{A} + \frac{\mathbb{B}\sqrt{cr^2\mathrm{e}^{anr^2}}}{anr}\right)^2\mathrm{d}t^2 \\ &+ \left(\frac{(1 + cr^2\mathrm{e}^{nar^2})(cr^2 + 1)}{(cr^2 + 1) + \beta ncr^2(1 + cr^2\mathrm{e}^{nar^2})}\right)\mathrm{d}r^2 \\ &+ r^2\left(\mathrm{d}\theta^2 + \sin^2\theta\mathrm{d}\phi^2\right),\end{aligned} \tag{37}$$

where

$$\mathrm{e}^{\nu(r)} = \left(\mathbb{A} + \frac{\mathbb{B}\sqrt{cr^2\mathrm{e}^{anr^2}}}{anr}\right)^2, \tag{38}$$

$$\mathrm{e}^{-\xi(r)} = \frac{(1 + cr^2\mathrm{e}^{nar^2})(cr^2 + 1)}{(cr^2 + 1) + \beta ncr^2(1 + cr^2\mathrm{e}^{nar^2})}. \tag{39}$$

In subsequent computations, the characterization of the total state quantities, that is, the energy density and the radial and tangential pressures will be implemented, as follows:

$$\rho^{(\text{total})} = \rho + \alpha\vartheta_0^0, \tag{40}$$

$$p_r^{(\text{total})} = p_r - \alpha\vartheta_1^1, \tag{41}$$

$$p_t^{(\text{total})} = p_t - \alpha\vartheta_2^2, \tag{42}$$

where density and pressure are given by Eqs. (21)−(23). These relations involve additional geometric quantities that interact via the coupling parameter α.

The quantities $\rho^{(\text{total})}$, along with $p_r^{(\text{total})}$ and $p_t^{(\text{total})}$ for completing the system, are expressed as follows:

$$\begin{aligned}
\rho^{\text{total}} &= \frac{1}{3k_1r^2(2\gamma+k_1)}\Bigg(\frac{1}{k_2r+1}\Bigg(\frac{4\mathrm{a}^2\mathbb{B}^2\gamma k_2^2n^2r^4}{k_3^2}+\frac{4\mathrm{a}\mathbb{B}\gamma n(k_2r)^{3/2}\left(\mathrm{a}\mathbb{A}nr\left(\mathrm{a}nr^2+1\right)+\mathbb{B}\sqrt{k_2r}\right)}{k_3^2}\\
&+\frac{2\mathrm{a}\mathbb{B}\gamma k_2nr^2\left(\frac{2\mathrm{a}nr^2+2}{k_2r+1}-2\mathrm{a}nr^2+2\right)}{k_3}+\frac{4k_2r\left(\mathrm{a}nr^2+1\right)(8\gamma+48\pi G+3\lambda)}{k_2r+1}+2k_2r(8\gamma+48\pi G+3\lambda)\Bigg)\\
&+\frac{2\beta\mathrm{c}nr^2}{(\mathrm{c}r^2+1)^2}\Bigg(\Bigg(k_2\left(-\mathrm{a}^2\mathbb{A}^2n^2r(8\gamma+3\lambda)\left(\mathrm{c}r^2+3\right)+2\mathrm{a}\mathbb{A}\mathbb{B}n\sqrt{k_2r}\Big(\gamma\Big(r^2\left(\mathrm{c}\left(\mathrm{a}nr^2\left(\mathrm{a}nr^2+3\right)-8\right)\right.\right.\right.\\
&\left.\left.\left.+\mathrm{a}n\left(\mathrm{a}nr^2+4\right)\right)-24\Big)-3\lambda\left(\mathrm{c}r^2+3\right)\Big)+\mathbb{B}^2k_2\Big(2\gamma\Big(r^2\left(\mathrm{a}nr^2+4\right)\left(\mathrm{ac}nr^2\right.\right.\\
&\left.\left.+\mathrm{a}n-\mathrm{c}\right)-12\Big)-3\lambda\left(\mathrm{c}r^2+3\right)\Big)\Big)\Big/\left(k_3^2\right)+48\pi G\left(\mathrm{c}r^2+3\right)\Bigg)\Bigg),\\
p_r^{\text{total}} &= \frac{1}{3k_1r^2(2\gamma+k_1)}\Bigg(\frac{1}{k_2r+1}\Bigg(-\frac{4\mathrm{a}^2\mathbb{B}^2\gamma k_2^2n^2r^4}{k_3^2}-\frac{4\mathrm{a}\mathbb{B}\gamma n(k_2r)^{3/2}\left(\mathrm{a}\mathbb{A}nr\left(\mathrm{a}nr^2+1\right)+\mathbb{B}\sqrt{k_2r}\right)}{k_3^2}\\
&+\frac{2\mathrm{a}\mathbb{B}k_2nr^2\left(2\gamma\left(-\frac{\mathrm{a}nr^2+1}{k_2r+1}+\mathrm{a}nr^2+11\right)+96\pi G+6\lambda\right)}{k_3}+\frac{16\gamma k_2r\left(\mathrm{a}nr^2+1\right)}{k_2r+1}-2k_2r(8\gamma\\
&+48\pi G+3\lambda)\Bigg)+\Bigg(\beta\mathrm{c}nr^2\Big(\Big(2\left(\mathrm{a}\mathbb{A}n\left(\mathrm{c}r^2+1\right)\sqrt{k_2r}(8\gamma+48\pi G+3\lambda)+\mathbb{B}k_2\left(48\pi G\left(\mathrm{c}r^2+1\right)\left(2\mathrm{a}nr^2+1\right)\right.\right.\right.\\
&\left.\left.\left.+2\gamma\left(r^2\left(\mathrm{c}\left(\mathrm{a}nr^2\left(9-\mathrm{a}nr^2\right)+4\right)+\mathrm{a}n\left(8-\mathrm{a}nr^2\right)\right)+4\right)+3\lambda\left(\mathrm{c}r^2+1\right)\left(2\mathrm{a}nr^2+1\right)\right)\Big)/(k_3)-16\gamma\Big)\Bigg)\\
&\Big/\left(\left(\mathrm{c}r^2+1\right)^2\right)\Bigg),\\
p_t^{\text{total}} &= \frac{\mathrm{c}}{3k_1(2\gamma+k_1)}\Bigg(\Bigg(2r\mathrm{e}^{\mathrm{a}nr^2}\Bigg(\mathrm{a}^2\mathbb{A}^2k_2n^2\left(-48G\left(\pi\mathrm{a}nr^2+\pi\right)+r^2\left(\frac{4\gamma k_2}{r}-\mathrm{a}n(4\gamma+3\lambda)\right)-3\lambda\right)\\
&+\mathrm{a}\mathbb{B}n\sqrt{k_2r}\left(-3(16\pi G+\lambda)k_{\frac{2}{r}}\left(\mathrm{a}nr^2+2\right)+\mathrm{a}n\left(48\pi G\left(\mathrm{a}nr^2+2\right)+\mathrm{a}nr^2(10\gamma+3\lambda)+6(3\gamma+\lambda)\right)+8\gamma k_2^2\right)\\
&+\mathbb{B}^2k_2\left(\frac{k_2\left(4\mathrm{a}\gamma nr^2-48\pi G-3\lambda\right)}{r}+\mathrm{a}n\left(48\pi G\left(\mathrm{a}nr^2+2\right)+\mathrm{a}nr^2(10\gamma+3\lambda)+6(3\gamma+\lambda)\right)+4\gamma k_2^2\right)\Bigg)\\
&\Big/\left(k_3^2(k_2r+1)^2\right)+\Bigg(\beta n\Bigg(\Bigg(2k_2\left(\mathrm{c}r^2+1\right)\Bigg(\mathrm{a}^3\mathbb{A}\mathbb{B}n^3r^4\sqrt{k_2r}(10\gamma+48\pi G+3\lambda)+\mathrm{a}^2n^2r\Bigg(-4\mathbb{A}^2\gamma\\
&+6\mathbb{A}\mathbb{B}r\sqrt{k_2r}(3\gamma+16\pi G+\lambda)+\mathbb{B}^2k_2r^3(10\gamma+48\pi G+3\lambda)\Bigg)+2\mathrm{a}\mathbb{B}n\left(3\mathbb{B}k_2r^2(3\gamma+16\pi G+\lambda)-4\mathbb{A}\gamma\sqrt{k_2r}\right)\\
&-4\mathbb{B}^2\gamma k_2\Bigg)\Bigg)\Big/\left(k_3^2\right)+\frac{2\mathrm{a}\mathbb{B}k_2nr^2(10\gamma+48\pi G+3\lambda)}{k_3}+8\gamma+96\pi G+6\lambda\Bigg)\Bigg)\Big/\left(\left(\mathrm{c}r^2+1\right)^2\right)\Bigg),
\end{aligned} \tag{43}$$

where

$$k_1 = s2\gamma+16\pi G+\lambda, \quad k_2 = \mathrm{c}r\mathrm{e}^{\mathrm{a}nr^2}, \quad k_3 = \mathrm{a}\mathbb{A}n\sqrt{k_2r}+\mathbb{B}k_2.$$

B. Boundary conditions and determination of constants: Israel-Darmois matching

Matching conditions are crucial for understanding the physical characteristics of any gravitational model by

aligning interior and exterior geometries across a hypersurface. This process is governed by two primary conditions:

- **Continuity of metric coefficients**: The metric components of both spacetimes must be continuous at the hypersurface. This constraint ensures that there is no discontinuity in the metrics across the boundary.

- **Extrinsic curvature matching**: The extrinsic curvatures of both spacetimes must be equal at the hypersurface. This requirement leads to the condition $p_r^{\rm eff}=0$, which implies that there is no difference in the tensor components of the stress energy across the boundary.

These conditions are essential for ensuring smooth transition and consistency across the interior and exterior geometries of any gravitational model. For this study, we selected the exterior Schwarzschild spacetime as follows:

$$\begin{aligned} {\rm d}s^2 =& -\left(1-\frac{2\mathcal{M}}{r}\right){\rm d}t^2+\left(1-\frac{2\mathcal{M}}{r}\right)^{-1}{\rm d}r^2 \\ &+r^2\left({\rm d}\theta^2+\sin^2\theta{\rm d}\phi^2\right). \end{aligned} \tag{44}$$

By equating the exterior spacetime metric with Eq. (37) and applying the continuity conditions for the metric potentials, we derive the following two relations:

$$ {\rm e}^{\nu(r)} = 1-\frac{2\mathcal{M}}{\mathcal{R}}, \tag{45}$$

$$ {\rm e}^{-\xi(r)} = 1-\frac{2\mathcal{M}}{\mathcal{R}}, \tag{46}$$

where the terms $\mathcal{M}$ and $\mathcal{R}$ refer to the total mass and radius of the compact star, respectively. The second form of continuity, in which the pressure vanishes at the boundary and hence allows stability in a true vacuum, is presented as follows:

$$ p_r^{\rm total}(r)|_{r=\mathcal{R}} = \left(p_r-\alpha\vartheta_1^1\right)|_{r=\mathcal{R}}=0. \tag{47}$$

By utilizing Eqs. (45)−(47) and re-arranging them with the appropriate substitutions, the values of the random constants $\mathbb{A}$, $\mathbb{B}$, and c can be obtained as follows:

$$\begin{aligned} \mathbb{A} =& -\frac{{\rm B}\sqrt{c\mathcal{R}^2{\rm e}^{an*\mathcal{R}^2}}+an\sqrt{\mathcal{R}}\sqrt{\mathcal{R}-2\mathcal{M}}}{an\mathcal{R}}, \\ \mathbb{B} =& \Big(\Big(c\sqrt{\mathcal{R}}\sqrt{\mathcal{R}-2\mathcal{M}}\big(c\mathcal{R}^2{\rm e}^{2an\mathcal{R}^2}\left(8\gamma\left(\beta c^2n\mathcal{R}^4-\left(c\mathcal{R}^2+1\right)^2\right)+48\pi G\left(c\mathcal{R}^2+1\right)\left(c\mathcal{R}^2(\beta n-1)-1\right)\right. \\ &\left.+3\lambda\left(c\mathcal{R}^2+1\right)\left(c\mathcal{R}^2(\beta n-1)-1\right)\right)+{\rm e}^{an\mathcal{R}^2}\left(8a\gamma n\left(c\mathcal{R}^3+\mathcal{R}\right)^2+16\beta\gamma c^2n\mathcal{R}^4+48\pi G\left(c\mathcal{R}^2+1\right)\right. \\ &\left.*\left(c\mathcal{R}^2(2\beta n-1)-1\right)+3\lambda\left(c\mathcal{R}^2+1\right)\left(c\mathcal{R}^2(2\beta n-1)-1\right)\right)+\beta n\left(48G\left(\pi c\mathcal{R}^2+\pi\right)+c\mathcal{R}^2(8\gamma+3\lambda)+3\lambda\right)\Big)\Big) \\ &/\Big(2\sqrt{c\mathcal{R}^2{\rm e}^{an\mathcal{R}^2}}\big(\gamma\big(\mathcal{R}^2\big(c\big(\beta c^2n\mathcal{R}^4{\rm e}^{2an\mathcal{R}^2}\left(\mathcal{R}^2\left(c\left(an\mathcal{R}^2-9\right)+an\right)-8\right)+c\mathcal{R}^2(\beta n+1)\left(an\mathcal{R}^2-9\right)\right. \\ &\left.+2{\rm e}^{an\mathcal{R}^2}\left(\beta cn\mathcal{R}^2\left(\mathcal{R}^2\left(c\left(an\mathcal{R}^2-9\right)+an\right)-8\right)-5\left(c\mathcal{R}^2+1\right)^2\right)+an\mathcal{R}^2(\beta n+2)-8\beta n-18\right)+an\big)-9\big) \\ &-48\pi G\left(c\mathcal{R}^2+1\right)\left(c\mathcal{R}^2{\rm e}^{an\mathcal{R}^2}+1\right)\left(c\mathcal{R}^2\left(\beta n\left(c\mathcal{R}^2{\rm e}^{an\mathcal{R}^2}+1\right)+1\right)+1\right)-3\lambda\left(c\mathcal{R}^2+1\right) \\ &*\left(c\mathcal{R}^2{\rm e}^{an\mathcal{R}^2}+1\right)\left(c\mathcal{R}^2\left(\beta n\left(c\mathcal{R}^2{\rm e}^{an\mathcal{R}^2}+1\right)+1\right)+1\right)\big)\big)\Big), \\ c =& \Big(4\mathcal{M}\Big)/\Big(-2\mathcal{M}\mathcal{R}^2\left({\rm e}^{an\mathcal{R}^2}+1\right)+\sqrt{\mathcal{R}^4\left(\left(-(\mathcal{R}-2\mathcal{M}){\rm e}^{an\mathcal{R}^2}+2\mathcal{M}+\beta n\mathcal{R}\right)^2-8\mathcal{M}{\rm e}^{an\mathcal{R}^2}(2\mathcal{M}+\mathcal{R}(\beta n-1))\right)} \\ &+\mathcal{R}^3\left({\rm e}^{an\mathcal{R}^2}-\beta n\right)\Big). \end{aligned} \tag{48}$$

Random constants $\mathbb{A}$, $\mathbb{B}$, and c are then evaluated by taking $\beta=0.2$ and $\beta=-0.2$, and the summary of resulting values is provided in Tables 1 and 2, in which the data of seven selected stellar models has been utilized. In both instances, the fixed parameters are $\lambda=1\times10^{-12}$, $a=0.03$, and $\gamma=0.009$, whereas the coupling parameter can assume any non-zero real value, as illustrated in the tables.

Utilizing the listed constant values for the selected stellar candidates, we generated plots of the metric potentials, as shown in Figs. 1(a) and 1(b). These figures illus-

Table 1. Synopsis of computed values of constants based on the data of seven stellar candidates for MGD case ($\beta = 0.2$, $\lambda = 1 * 10^{-12}$, $a = 0.03$, $\gamma = 0.009$).

Star Models	Mass $\mathcal{M}/\mathcal{M}_{\odot}$	Radius $\mathcal{R}$(km)	Mass-radius($\frac{\mathcal{M}}{\mathcal{R}}$)	c	$\mathbb{B}$	$\mathbb{A}$
Her X-1 [69]	0.85±0.15	8.1±0.41	0.154	0.00339865	−0.0279575	−0.289412
LMC X-4 [70]	1.04±0.09	8.301±0.2	0.184	0.00403809	−0.029791	−0.165948
Cen X-3 [71]	1.49±0.08	9.178±0.13	0.239	0.00454612	−0.0306402	−0.0403881
4U 1608-52 [72]	1.74±0.14	9.528±0.15	0.269	0.0049576	−0.03128	0.0445229
Vela X-1	1.77±0.08	9.56±0.08	0.273	0.00502456	−0.0312868	0.057035
PSR J1614-2230 [73]	1.97±0.04	9.69±0.2	0.300	0.0056665	−0.0324197	0.166191
PSR J0740+6620 [74]	2.07±0.04	12.34±0.2	0.247	0.00214646	−0.02322001	−0.3364949

Table 2. Synopsis of computed values of constants based on the data of seven star models for MGD case ($\beta = -0.2$, $\lambda = 1 * 10^{-12}$, $a = 0.03$, $\gamma = 0.009$).

Star Models	Mass $\mathcal{M}/\mathcal{M}_{\odot}$	Radius $\mathcal{R}$(km)	Mass-radius($\frac{\mathcal{M}}{\mathcal{R}}$)	c	$\mathbb{B}$	$\mathbb{A}$
Her X-1 [69]	0.85±0.15	8.1±0.41	0.154	0.00325493	−0.028568	−0.289414
LMC X-4 [70]	1.04±0.09	8.301±0.2	0.184	0.0038583	−0.0304771	−0.165951
Cen X-3 [71]	1.49±0.08	9.178±0.13	0.239	0.00432607	−0.0314096	−0.0403919
4U 1608-52 [72]	1.74±0.14	9.528±0.15	0.269	0.00470364	−0.0321131	0.0445179
Vela X-1	1.77±0.08	9.56±0.08	0.273	0.00476514	−0.0322297	0.0570297
PSR J1614-2230 [73]	1.97±0.04	9.69±0.2	0.300	0.00535511	−0.0333488	0.166184
PSR J0740+6620 [74]	2.07±0.04	12.34±0.2	0.247	0.00205513	−0.0237099	−0.364951

trate the trend of the metric potentials as functions of the radial coordinate r for two distinct constant values across the four stellar models. In both cases, the metric potentials exhibit regular, monotonically increasing, and finite behavior throughout the stellar interior, without any indication of singularities.

IV. PHYSICAL ANALYSIS

In this section, we analyze the stability of our solutions by exploring various physical characteristics that are crucial for the validity and stability of celestial objects in any gravitational framework. This includes the illustration of the energy density, pressures (p_r, p_t), and their gradients, anisotropy, velocities, equation of state (EoS), mass, compactness, and redshift. All of these measures are explained in detail in the following subsections.

A. Energy density, pressures, and gradients

In self-gravitating bodies—particularly highly dense objects such as compact objects and matter components—the energy density and pressures are anticipated to exhibit characteristic behavior. The energy density and pressures are expected to be maximum at the core of the star, showing finite, positive, and singularies-free behavior, which decreases toward the surface. This behavior supports the stability of the model within the proposed theoretical framework. Figures 2 and 3 illustrate the radial profiles of energy density, as well as the tangential and radial pressures, throughout the radius of the compact star models. The tangential pressure vanishes at the boundary. Furthermore, we analyzed the gradients of the energy density and pressure, which are essential for the construction of a compact star model. It has been posited [75] that these gradients must exhibit negative behavior. We conducted this analysis by considering two specific cases: first, by varying the parameter n while keeping the coupling parameter β constant, and second, by varying β while maintaining a constant value for n. This examination ensures the consistency of our model under the following conditions in both scenarios:

$$\frac{\mathrm{d}\rho}{\mathrm{d}r} < 0; \quad \frac{\mathrm{d}p_r}{\mathrm{d}r} < 0; \quad \frac{\mathrm{d}p_t}{\mathrm{d}r} < 0. \tag{49}$$

Figures 3(b) and 3(c) illustrate the behavior of all gradients in both scenarios. The gradients were in accordance with the essential conditions, exhibited a decreasing trend, and vanished at the stellar core, that is, at $r = 0$. This behavior is consistent with the physical expectations of a compact star model, where the energy density and pressures reach their maximum at the center and decrease outward.

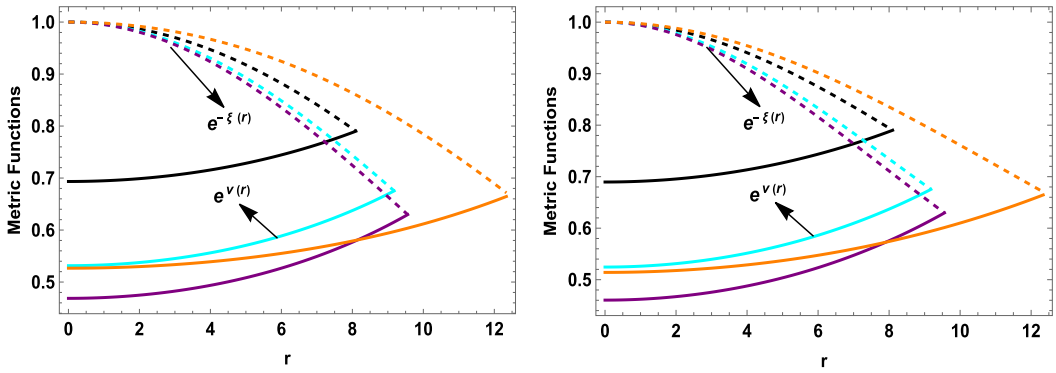

(a)With $\gamma = 0.009,\ a = 0.03,\ n = 0.1,\ \beta = 0.2$ (b)With $\gamma = 0.0009,\ a = 0.0003,\ n = 2,\ \beta = 0.01$

Fig. 1. (color online) For the compact star Her X-1 ($\mathcal{M}/\mathcal{M}_\odot = 0.85$, $\mathcal{R} = 8.1$)(■), Cen X-3 ($\mathcal{M}/\mathcal{M}_\odot = 1.49$, $\mathcal{R} = 9.178$)(■), Vela X-1 ($\mathcal{M}/\mathcal{M}_\odot = 1.77$, $\mathcal{R} = 9.56$)(■) and PSR J0740+6620 ($\mathcal{M}/\mathcal{M}_\odot = 2.07$, $\mathcal{R} = 12.34$)(■), the variations in metric functions against r are shown. All plots use $\lambda = 1 \times 10^{-12}$.

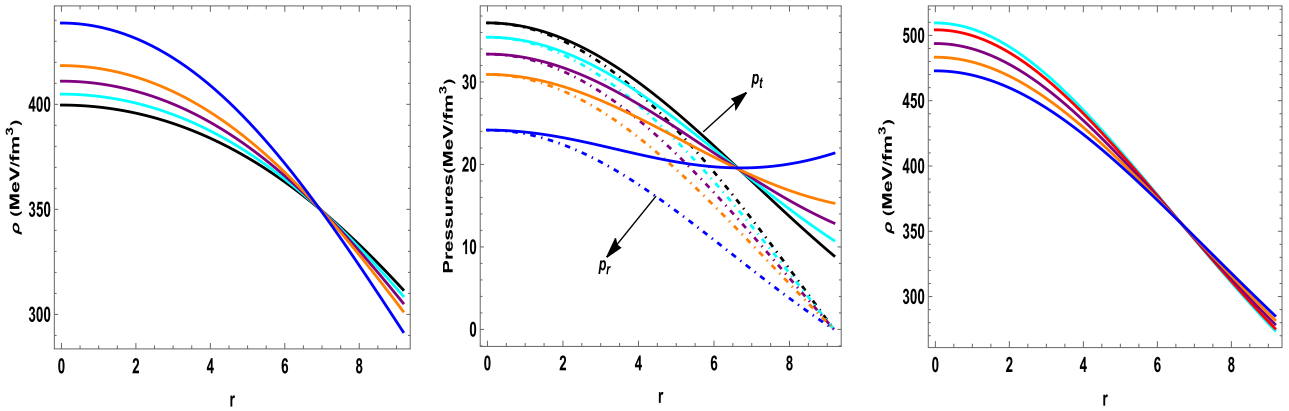

(a)For β variations with $\gamma = 0.009,\ a = 0.03$ (b)For β variations with $\gamma = 0.009,\ a = 0.03$ (c)For n variations with $\gamma = 0.0009,\ a = 0.0003$

Fig. 2. (color online) For the compact star Cen X-3 ($\mathcal{M}/\mathcal{M}_\odot = 1.49$, $\mathcal{R} = 9.178$), the variations in energy density and pressures with the radial coordinate r are shown. Subfigures (a) and (b) depict energy density and pressures (p_t & p_r) for $n = 0.1$ with $\beta = 0$ (■), $\beta = 0.5$ (■), $\beta = 1$ (■), $\beta = 1.5$ (■), and $\beta = 2.5$ (■). Subfigure (c) shows energy density for $\beta = 0.01$ with $n = 0.5$ (■), $n = 1$ (■), $n = 2$ (■), $n = 3$ (■), and $n = 4$ (■). All plots use $\lambda = 1 \times 10^{-12}$.

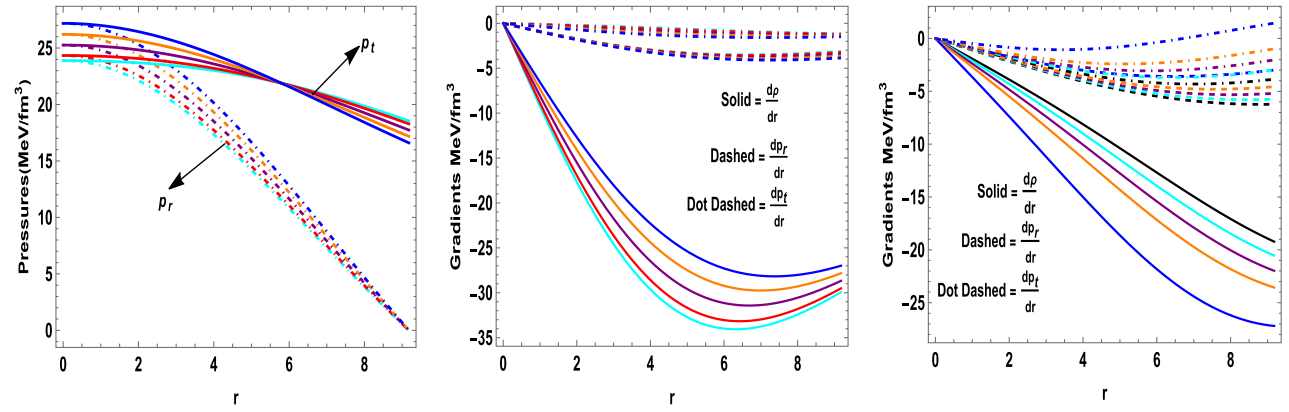

(a)For n variations with $\gamma = 0.0009,\ a = 0.0003$ (b)For n variations with $\gamma = 0.0009,\ a = 0.0003$ (c)For β variations with $\gamma = 0.009,\ a = 0.03$

Fig. 3. (color online) For the compact star Cen X-3 ($\mathcal{M}/\mathcal{M}_\odot = 1.49$, $\mathcal{R} = 9.178$), the variations in pressures and gradients with the radial coordinate r are shown. Subfigures (a) and (b) depict pressures (p_t & p_r) and gradients for $\beta = 0.01$ with $n = 0.5$ (■), $n = 1$ (■), $n = 2$ (■), $n = 3$ (■), and $n = 4$ (■). Subfigure (c) shows gradients for $n = 0.1$ with $\beta = 0$ (■), $\beta = 0.5$ (■), $\beta = 1$ (■), $\beta = 1.5$ (■), and $\beta = 2.5$ (■). All plots use $\lambda = 1 \times 10^{-12}$.

$$\left.\frac{\mathrm{d}\rho}{\mathrm{d}r}\right|_{r=0}=0;\quad \left.\frac{\mathrm{d}p_r}{\mathrm{d}r}\right|_{r=0}=0;\quad \left.\frac{\mathrm{d}p_t}{\mathrm{d}r}\right|_{r=0}=0. \tag{50}$$

B. Anisotropy, energy conditions, and equilibrium forces

Pressure anisotropy is a crucial factor in assessing the stability of a compact object, because it provides valuable insights into the interior stellar structure. For a stable compact star, the anisotropy—denoted by Δ—should be non-zero. When the tangential pressure p_t exceeds the radial pressure p_r, anisotropy Δ is positive ($\Delta>0$) and exhibits a repulsive (outward-directed) force. Conversely, if p_r is greater than p_t, anisotropy is negative ($\Delta<0$) and refers to an attractive (inward-directed) force [76]. Figures 4(c) and 5(c) demonstrate the behavior of anisotropy as a function of radius. The anisotropy is zero at the core and becomes positive, increasing toward the boundary in both cases, as shown graphically. This trend confirms the repulsive trend of anisotropy and the necessary anti-gravitational behavior of the anisotropic force to maintain the stability of the stellar structures.

Energy conditions represent mathematical constraints on the energy-momentum tensor of self-gravitating bodies and form the root cause of singularity theorems [77] and entropy bounds [78]. These conditions are pivotal for

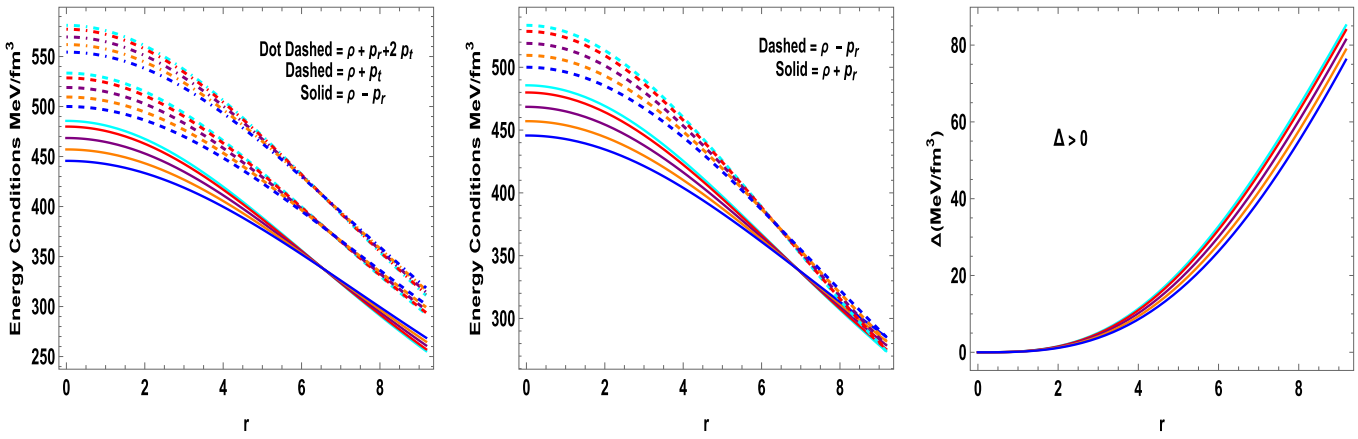

(a)For n variations with $\gamma=0.0009,\ a=0.0003$ (b)For n variations with $\gamma=0.0009,\ a=0.0003$ (c)For β variations with $\gamma=0.009,\ a=0.03$

Fig. 4. (color online) For the compact star Cen X-3 ($\mathcal{M}/\mathcal{M}_\odot=1.49$, $\mathcal{R}=9.178$), the variations in energy conditions and anisotropy with the radial coordinate r are shown. Subfigures (a) and (b) depict energy conditions and (c) depicts anisotropy for $\beta=0.01$ with $n=0.5$ (■), $n=1$ (■), $n=2$ (■), $n=3$ (■), and $n=4$ (■). All plots use $\lambda=1\times10^{-12}$.

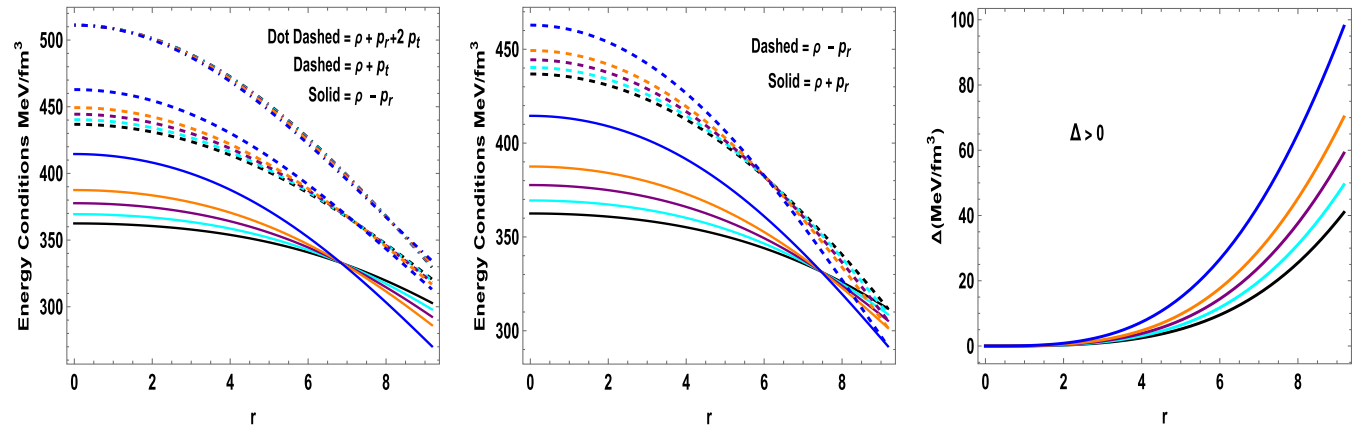

(a)For β variations with $\gamma=0.009,\ a=0.03$ (b)For β variations with $\gamma=0.009,\ a=0.03$ (c)For n variations with $\gamma=0.0009,\ a=0.0003$

Fig. 5. (color online) For the compact star Cen X-3 ($\mathcal{M}/\mathcal{M}_\odot=1.49$, $\mathcal{R}=9.178$), the variations in energy conditions and anisotropy with the radial coordinate r are shown. Subfigures (a) and (b) depict energy conditions and (c) depicts anisotropy for $n=0.1$ with $\beta=0$ (■), $\beta=0.5$ (■), $\beta=1$ (■), $\beta=1.5$ (■), and $\beta=2.5$ (■). All plots use $\lambda=1\times10^{-12}$.

assessing the feasibility of relativistically stable models. The primary energy conditions include the strong energy condition (SEC), weak energy condition (WEC), null energy condition (NEC), and dominant energy condition (DEC). Mathematically, these are as follows:

$$\begin{aligned}
&\textbf{NEC}: \rho^{\text{eff}} \geq 0, \\
&\textbf{WEC}: \rho^{\text{eff}} + p_t^{\text{eff}} \geq 0, \qquad \rho^{\text{eff}} + p_r^{\text{eff}} \geq 0. \\
&\textbf{SEC}: \rho^{\text{eff}} + 2p_t^{\text{eff}} + p_r^{\text{eff}} \geq 0, \\
&\textbf{DEC}: \rho^{\text{eff}} - |p_r^{\text{eff}}| \geq 0, \qquad \rho^{\text{eff}} - |p_t^{\text{eff}}| \geq 0.
\end{aligned} \tag{51}$$

For a physically captivating model, the associated inequalities must be satisfied to ensure that these energy conditions reach their maximum at the core of the star and remain positive throughout its structure. As shown in Figs. 4(a), 4(b), 5(a), and 5(b), all specified energy conditions are met under both scenarios: when varying the parameter n while keeping the coupling parameter β constant and when varying β while maintaining n constant. This consistency across both cases further validates the stability of the proposed models.

Next, we analyze the equilibrium conditions through the involved forces, that is, the gravitational force (F_g), hydrostatic force (F_h), anisotropic force (F_a) and modified force (F_m) due to our modified $f(\mathcal{R},T,\mathcal{L}_m)$ gravity model. By incorporating the effects of the MGD approach, the extended Tolman-Oppenheimer-Volkoff (TOV) equation for our model is formulated as follows:

$$\underbrace{-\frac{H(r)'}{2}\left[\rho + p_r + \beta(\vartheta_0^0 - \vartheta_1^1)\right]}_{F_g} \underbrace{-\left(\frac{\mathrm{d}p_r}{\mathrm{d}r} - \beta\frac{\mathrm{d}\vartheta_1^1}{\mathrm{d}r}\right)}_{F_h} \underbrace{+\frac{2}{r}\left[p_r - p_r - \beta(\vartheta_0^0 - \vartheta_1^1)\right]}_{F_a}$$
$$\underbrace{+\frac{\mathrm{d}}{\mathrm{d}r}\left[\frac{\gamma}{6(8\pi G + \gamma + \lambda/2)}\left((3\rho - p_r - 2p_t) + \beta(3\vartheta_0^0 + \vartheta_1^1 + 2\vartheta_2^2)\right]\right)}_{F_m} = 0. \tag{52}$$

To ensure the stability of our model within $f(\mathcal{R},T,\mathcal{L}_m)$ gravity, the total impact of all forces, that is, gravitational (F_g), hydrostatic (F_h), anisotropic (F_a), and modified force (F_m), must be zero, which implies that these forces are in equilibrium. This balancing effect ensures the stability of all configurations. Figures 6(a) and 6(b) show the behavior of these forces in two distinct scenarios. In the first scenario, the parameters are held constant and the forces are plotted as functions of varying n, as depicted in Fig. 6(a). The figure shows that the gravitational force is counteracted by combined hydrostatic and anisotropic forces, which act in opposite directions. This equilibrium prevents gravitational collapse, whereas the modified force remains constant and exerts only a small

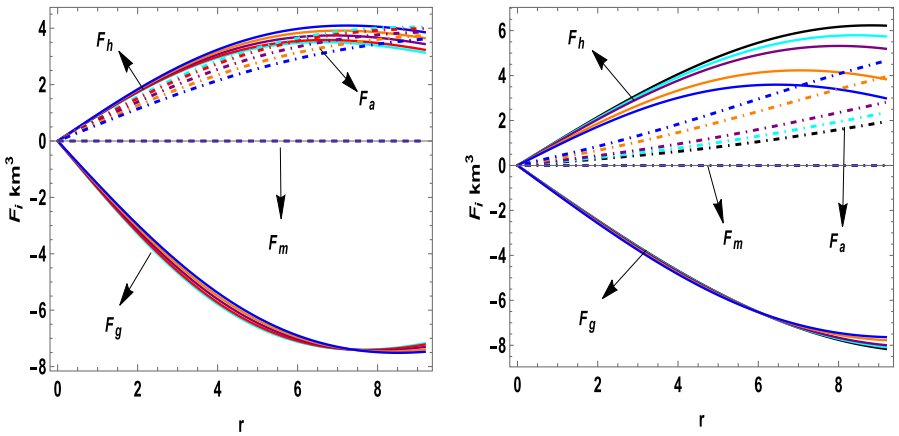

(a)[For n variations with $\gamma = 0.0009,\ a = 0.0003$ (b)For β variations with $\gamma = 0.009,\ a = 0.03$

Fig. 6. (color online) For the compact star Cen X-3 ($\mathcal{M}/\mathcal{M}_\odot = 1.49$, $\mathcal{R} = 9.178$), the variations in forces with the radial coordinate r are shown. Subfigure (a) depict forces for $\beta = 0.01$ with $n = 0.5$ (■), $n = 1$ (■), $n = 2$ (■), $n = 3$ (■), and $n = 4$ (■). Subfigure (b) shows forces for $n = 0.1$ with $\beta = 0$ (■), $\beta = 0.5$ (■), $\beta = 1$ (■), $\beta = 1.5$ (■), and $\beta = 2.5$ (■). All plots use $\lambda = 1 \times 10^{-12}$.

impact on the hydrostatic balance. In the second scenario, the forces were plotted for varying values of the coupling parameter β, as illustrated in Fig. 6(b). This figure confirms that even with different values of β, all the forces are balanced, which further confirms the stability of the model. These findings confirm that the model is not only stable but also represents a physically viable relativistic system.

C. Equation of state and stability analysis

The equation of state represents a dimensionless constraint on the parameters governing radial and tangential pressures. These limitations play a pivotal role in establishing the relationship between the state variables, as expressed by the following equation:

$$\omega_t = \frac{p_t}{\rho}, \quad \omega_r = \frac{p_r}{\rho}. \tag{53}$$

It is posited that both parameters must lie between 0 and 1 to ensure the physical stability of a relativistic model and confirm the non-exotic nature of the internal fluid distribution [79]. Figures 7(a) and 7(b) depict the trends of these parameters along the radial direction, with ω_r vanishing at the star boundary for two scenarios—varying n and β—as labeled in the figures. The results clearly demonstrate that both EoS parameters fall within the aforementioned limits, thereby confirming that the solutions are physically viable and consistent with the stable relativistic star models.

The pressure components must be constrained by the speed of light [80] to evaluate the physical stability of the anisotropic compact star models. This is achieved using Herrera's concept of cracking [81], which defines the expressions for the tangential and radial velocities, as outlined below. Both velocities must lie within the range $[0,1]$, as shown below, which is a requirement termed the causality condition:

$$v_r^2 = \frac{\mathrm{d}p_r}{\mathrm{d}\rho}, \quad v_t^2 = \frac{\mathrm{d}p_t}{\mathrm{d}\rho}. \tag{54}$$

The concept of cracking was further extended by Abreu [82] and Andreasson [83] to assess the stability of stellar structures. This extension is represented by the following equations and inequalities. For a model to be physically promising and potentially stable, it must adhere to the conditions outlined below:

$$= \begin{cases} -1 \le v_t^2 - v_r^2 \le 0, & \text{Potentially stable;} \\ 0 < v_t^2 - v_r^2 \le 1, & \text{Potentially unstable.} \end{cases} \tag{55}$$

Figures 8(a), 8(b), 8(c), and 9(a) illustrate the radial and tangential velocities (v_r^2 and v_t^2) and their differences. As shown, the velocities remain within the specified regions for both scenarios—varying β and n—which confirms the stability of our models. These results reinforce the physical viability and consistency of the model and further validates its capacity to represent a stable relativistic system.

D. Adiabatic index

The adiabatic index, which describes the stiffness of the EoS by measuring the change in pressure in response to slight variations in matter density, is a critical factor in analyzing the stability of stellar structures, both relativistically and non-relativistically. Chandrasekhar [84] noted

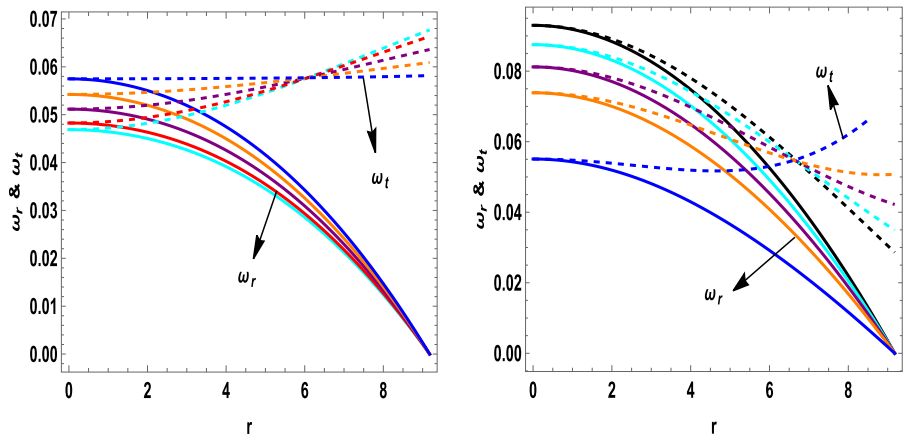

(a)[For n variations with $\gamma = 0.0009$, $a = 0.0003$ (b)For β variations with $\gamma = 0.009$, $a = 0.03$

Fig. 7. (color online) For the compact star Cen X-3 ($\mathcal{M}/\mathcal{M}_\odot = 1.49$, $\mathcal{R} = 9.178$), the variations in EoS with the radial coordinate r are shown. Subfigure (a) EoS(w_t & w_r) for $\beta = 0.01$ with $n = 0.5$ (■), $n = 1$ (■), $n = 2$ (■), $n = 3$ (■), and $n = 4$ (■). Subfigure (b) shows EoS(w_t & w_r) for $n = 0.1$ with $\beta = 0$ (■), $\beta = 0.5$ (■), $\beta = 1$ (■), $\beta = 1.5$ (■), and $\beta = 2.5$ (■). All plots use $\lambda = 1 \times 10^{-12}$.

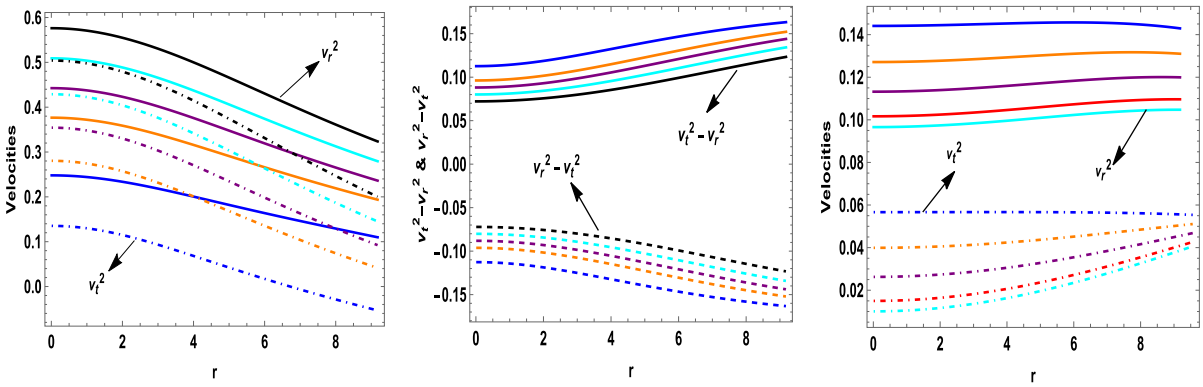

(a)For β variations with $\gamma = 0.009,\ a = 0.03$ (b)For β variations with $\gamma = 0.009,\ a = 0.03$ (c)For n variations with $\gamma = 0.0009,\ a = 0.0003$

Fig. 8. (color online) For the compact star Cen X-3 ($\mathcal{M}/\mathcal{M}_\odot = 1.49$, $\mathcal{R} = 9.178$), the variations in velocities and velocities difference with the radial coordinate r are shown. Subfigures (a) and (b) depict velocities (v_t^2 & v_r^2) and velocities difference ($v_t^2 - v_r^2$ & $v_r^2 - v_t^2$) for $n = 0.1$ with $\beta = 0$ (■), $\beta = 0.5$ (■), $\beta = 1$ (■), $\beta = 1.5$ (■), and $\beta = 2.5$ (■). Subfigure (c) shows velocities (v_t^2 & v_r^2) for $\beta = 0.01$ with $n = 0.5$ (■), $n = 1$ (■), $n = 2$ (■), $n = 3$ (■), and $n = 4$ (■). All plots use $\lambda = 1 \times 10^{-12}$.

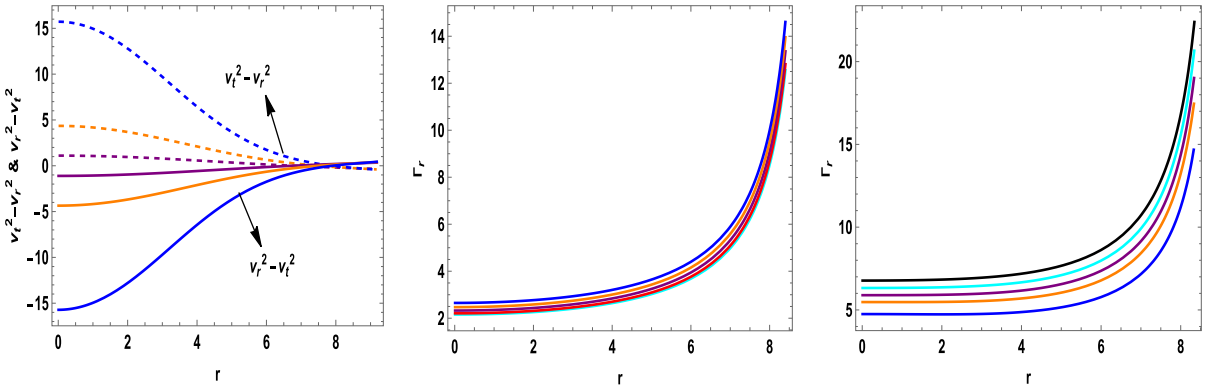

(a)[For n variations with $\gamma = 0.0009,\ a = 0.0003$ (b)[For n variations with $\gamma = 0.0009,\ a = 0.0003$ (c)For β variations with $\gamma = 0.009,\ a = 0.03$

Fig. 9. (color online) For the compact star Cen X-3 ($\mathcal{M}/\mathcal{M}_\odot = 1.49$, $\mathcal{R} = 9.178$), the variations in velocities difference and adiabatic index (Γ_r) with the radial coordinate r are shown. Subfigures (a) and (b) depict the velocities difference ($v_t^2 - v_r^2$ & $v_r^2 - v_t^2$) and adiabatic index for $\beta = 0.01$ with $n = 0.5$ (■), $n = 1$ (■), $n = 2$ (■), $n = 3$ (■), and $n = 4$ (■). Subfigure (c) shows adiabtic index for $n = 0.1$ with $\beta = 0$ (■), $\beta = 0.5$ (■), $\beta = 1$ (■), $\beta = 1.5$ (■), and $\beta = 2.5$ (■). All plots use $\lambda = 1 \times 10^{-12}$.

that the adiabatic index should adhere to $\Gamma > 4/3$, a criterion that has been extensively examined by various authors for both isotropic and anisotropic stellar models [85–86]. The adiabatic indices corresponding to the radial and tangential components are as follows:

$$\Gamma_r = \frac{\rho + p_r}{p_r}\left(\frac{\mathrm{d}p_r}{\mathrm{d}\rho}\right) = \frac{\rho + p_r}{p_r} v_r^2, \tag{56}$$

$$\Gamma_t = \frac{\rho + p_t}{p_t}\left(\frac{\mathrm{d}p_t}{\mathrm{d}\rho}\right) = \frac{\rho + p_t}{p_t} v_t^2. \tag{57}$$

Figures 9(b) and 9(c) illustrate the conduct of the adiabatic index Γ_r, demonstrating that its value consistently exceeds 4/3 in both scenarios when varying β and n. This result confirmed the stability of the model under these conditions. The adiabatic index Γ_t was not plotted, as it does not lead to any significant physical insight in this context. Additionally, Moustakidis [87] discussed the critical value of the adiabatic index Γ, emphasizing its strong dependence on the mass-to-radius ratio ($\mathcal{M}/\mathcal{R}$). The critical values of Γ for the seven different stellar candidates are listed in Tables 3 and 4. For all the stellar candidates, $\Gamma_{\rm crit}$ exceeds 4/3. The calculation of $\Gamma_{\rm crit}$ incorporates the modified mass resulting from gravitational decoupling. These findings further confirmed the stability and physical consistency of our models.

$$\Gamma_{\rm crit} = \frac{4}{3} + \frac{19}{42}\frac{2\mathcal{M}}{\mathcal{R}}. \tag{58}$$

Table 3. Synopsis of total mass along with compactness factor values by utilizing the MGD contribution for parameters ($\beta = 0.2$, $\lambda = 1 * 10^{-12}, a = 0.03, \gamma = 0.009$).

Star objects	$M_0/\mathcal{M}_\odot$	$\mathcal{R}$(km)	$u_0 = M_0/\mathcal{R}$	z_s	$M/\mathcal{M}_\odot$	$u = M/\mathcal{R}$	z_s(MGD)	$\Gamma_{\rm crit}(MGD)$
Her X-1 [69]	0.85	8.1	0.155	0.203153	0.839975	0.152772	0.19999	1.47156
LMC X-4 [70]	1.04	8.301	0.185	0.259026	1.02773	0.182395	0.254704	1.49836
Cen X-3 [71]	1.49	9.178	0.239	0.384532	1.47275	0.236397	0.377241	1.54722
4U 1608-52 [72]	1.74	9.528	0.269	0.471337	1.71993	0.265932	0.461549	1.57394
Vela X-1	1.77	9.56	0.278	0.483339	1.74958	0.269611	0.473173	1.57727
PSR J1614-2230 [73]	1.97	9.69	0.300	0.579186	1.94716	0.296032	0.565684	1.60117
PSR J0740+6620 [74]	2.07	12.34	0.247	0.406152	2.04937	0.244662	0.399352	1.55469

Table 4. Synopsis of total mass along with compactness parameter values by taking the MGD contribution for parameters ($\beta = -0.2$, $\lambda = 1 * 10^{-12}, a = 0.03, \gamma = 0.009$).

Star objects	$M_0/\mathcal{M}_\odot$	$\mathcal{R}$(km)	$u_0 = M_0/\mathcal{R}$	z_s	$M/\mathcal{M}_\odot$	$u = M/\mathcal{R}$	z_s(MGD)	$\Gamma_{\rm crit}(MGD)$
Her X-1 [69]	0.85	8.1	0.155	0.203153	0.859676	0.156355	0.206229	1.4748
LMC X-4 [70]	1.04	8.301	0.185	0.259026	1.05183	0.186672	0.263238	1.50223
Cen X-3 [71]	1.49	9.178	0.239	0.384532	1.50664	0.241837	0.391676	1.55214
4U 1608-52 [72]	1.74	9.528	0.269	0.471337	1.75935	0.272028	0.480962	1.57945
Vela X-1	1.77	9.56	0.278	0.483339	1.78969	0.275792	0.493341	1.58286
PSR J1614-2230 [73]	1.97	9.69	0.300	0.579186	1.99201	0.302851	0.59253	1.60734
PSR J0740+6620 [74]	2.07	12.34	0.247	0.406152	2.08997	0.249509	0.412826	1.55908

E. Mass function, compactness factor, and redshift function

In this section, we discuss the inter-connection between the mass function, compactness, and redshift because these quantities are inherently related. It is well known that the mass function must exhibit a positive increasing behavior and be consistent with the radial coordinate limit, that is, $r \to 0$, $\mathbb{M}(r) \to 0$. The mass reaches its maximum value at the boundary when $r = \mathcal{R}$. However, as previously discussed, gravitational decoupling introduces an additional gravitational source that affects the mass function. Therefore, the modified mass function for the current theory is given by

$$\mathbb{M}(r) = 4\pi \int_0^r \rho^{\rm eff}(r_1) {r_1}^2 \, {\rm d}r_1 = 4\pi \int_0^r [\rho(r_1) + \beta \vartheta_0^0(r_1)] {r_1}^2 \, {\rm d}r_1, \tag{59}$$

or

$$\mathbb{M}(r) = \frac{r}{2}\left(1 - {\rm e}^{-a(r)}\right) = \frac{r}{2}\left(1 - {\rm e}^{-W(r)} - \beta\psi(r)\right). \tag{60}$$

This modification to the mass relation reflects the impact of supplemental gravitational contributions resulting from the decoupling process, which further affects the structure and dynamics of the compact object. The revised equation can be expressed as follows, with the first component representing the mass at $r = \mathcal{R}$ derived solely from $f(\mathcal{R}, \mathcal{L}_m, T)$ gravity, as follows:

$$M = M_0 - \beta \frac{\mathcal{R}}{2}\psi(\mathcal{R}), \quad \text{where} \quad M_0 = \frac{\mathcal{R}}{2}(1 - {\rm e}^{-W(r)}). \tag{61}$$

This formulation sets forth the contributions from the standard $f(\mathcal{R}, \mathcal{L}_m, T)$ gravity from those introduced by gravitational decoupling. The compactness factor [88] for $f(\mathcal{R}, \mathcal{L}_m, T)$ gravity owing to the MGD approach can be written as

$$u^{\rm eff} = \frac{M}{\mathcal{R}} = u_0 - \frac{\beta}{2}\psi(\mathcal{R}), \quad \text{where} \quad u_0 = \frac{M_0}{\mathcal{R}}. \tag{62}$$

Owing to the impact of the compactness $u^{\rm eff}$, the surface gravitational redshift z_s is also influenced by the decoupling process. Thus, the modified surface redshift z_s in the context of the MGD for $f(\mathcal{R}, \mathcal{L}_m, T)$ gravity is expressed as follows [89] :

$$z_s = \left(1 - 2u_0 + \beta\psi(\mathcal{R})\right)^{-1/2} - 1. \tag{63}$$

Following the discussion of mass, redshift, and compactness under the gravitational decoupling effect, a few key

points can be outlined from the graphical analysis.

- First, mass expansion can be achieved using the MGD technique [90] within $f(\mathcal{R},\mathcal{L}_m,T)$ gravity. As seen from Eq. (61), if the second term is positive, then the overall mass increases. In our case, this is possible for negative values of the interaction parameter β. As the mass increases, both the redshift (z_s) and compactness (u) increase. Various authors have previously achieved similar results, as seen in [64], where mass expansion is observed for negative β, whereas in [91–92], the authors reported mass expansion for positive coupling parameter values. Tables 3 and 4 display the values of mass, redshift, and compactness with and without the coupling effect for both negative and positive β values across the seven star candidates. Notably, the mass increases only for positive β values, whereas for negative β, the modified mass is less than the original. Additionally, the critical values of the adiabatic index obtained using Eq. (58) for the modified mass using the MGD approach are shown in the table for all stars. The value is greater than 4/3 in both cases (positive and negative β values), confirming the stable trend of the proposed model within the realm of $f(\mathcal{R},\mathcal{L}_m,T)$ gravity. Moreover, Figs. 10 and 11 show plots of the modified mass, redshift, and compactness for both cases.

- Second, the modified compactness due to MGD is greater compared to compactness without this effect. Our findings are also consistent with the Buchdahl limits [93] for isotropic ($u \le 4/9$) and anisotropic fluids ($u \le 0.30$), which are crucial for establishing a physically acceptable model.

Table 5 presents a clear comparative analysis of the various anisotropic stellar models developed within different modified gravity frameworks. It highlights the distinct features of each model and illustrates how the

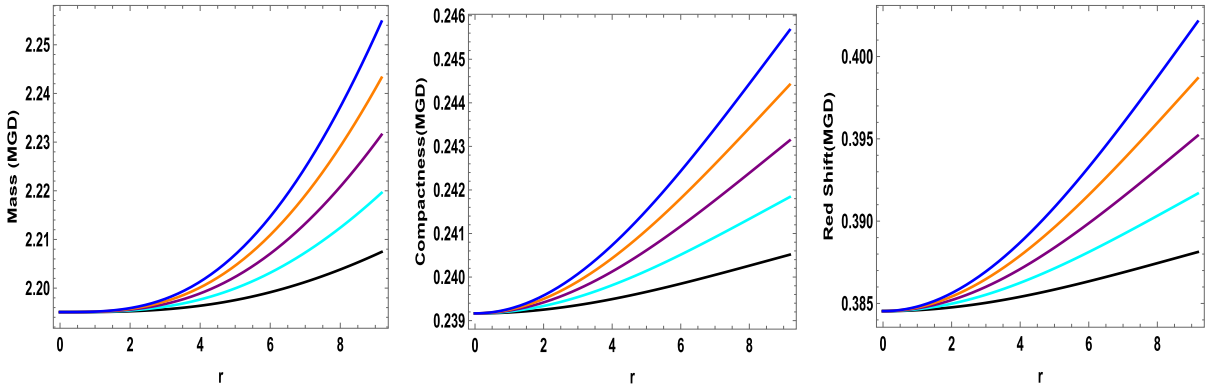

Fig. 10. (color online) For the compact star Cen X-3 ($\mathcal{M}/\mathcal{M}_\odot = 1.49$, $\mathcal{R} = 9.178$), the plots show how the mass function, compactness, and redshift vary with the radial coordinate r. The variation is considered for some variations of β: $\beta = -0.1$ (■), $\beta = -0.2$ (■), $\beta = -0.3$ (■), $\beta = -0.4$ (■), and $\beta = -0.5$ (■). In all plots, the parameters are set to $\beta = 0.01$, $a = 0.03$, $\gamma = 0.009$, and $\lambda = 1 \times 10^{-12}$.

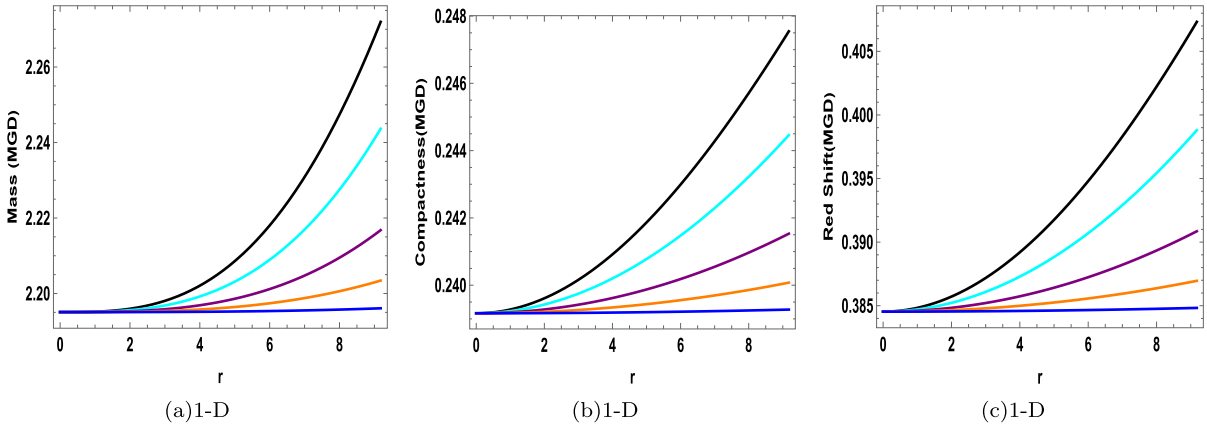

Fig. 11. (color online) For the compact star Cen X-3 ($\mathcal{M}/\mathcal{M}_\odot = 1.49$, $\mathcal{R} = 9.178$), the plots show how the mass function, compactness, and redshift vary with the radial coordinate r. The variation is considered for some values of n: $n = 0.5$ (■), $n = 1$ (■), $n = 1.5$ (■), $n = 2$ (■), and $n = 3$ (■). In all plots, the parameters are set to $n = 0.1$, $a = 0.0003$, $\gamma = 0.0009$, and $\lambda = 1 \times 10^{-12}$.

Table 5. Comparison of anisotropic stellar models in various modified gravity frameworks.

Gravity theory	Metric Anstaz	Matter Configuration	Stability & Features
$f(\mathcal{R},T)$ [94]	Krori-Barua metric	Anisotropic fluid	Physically acceptable; matched with Schwarzschild exterior; consistent graphs for real stars
$f(\mathcal{T})$ [95] gravity	Krori-Barua metric	Anisotropic fluid	Regular and stable; consistent with 4U 1820-30, Her X-1, and SAX J1808.4-3658; surface redshift analyzed
$f(\mathcal{R},\mathcal{L}_m,T)=\mathcal{R}+\alpha T\mathcal{L}_m$ [96]	Numerical (non-KB)	Anisotropic quark matter; MIT bag model	Mass–radius relation, adiabatic index, sound speed; α constrained using observational data
$f(\mathcal{R},\mathcal{L}_m,T)$ **Present Work**	Class-1 embedding; MGD approach	Anisotropic fluid; radial metric deformation	Well-behaved energy density/pressures; negative β yields higher mass; stability via TOV and Herrera cracking condition

present study based on Class-I solutions within the MGD approach relates to and extends previous works. By adopting a more generalized gravitational theory, namely $f(R,L_m,T)$, which encompasses earlier special cases, and by utilizing realistic values of mass and radius of compact stars, the model offers a physically consistent anisotropic extension of an initially isotropic seed solution. This comparative framework emphasizes the novelty and physical viability of the present model within the broader context of modified gravity theories.

It is important to note that mass–radius (M–R) curves provide the most direct diagnostic of stellar configurations. In the present analysis, we fixed the stellar mass and adopted the assumed radii to examine the physical behavior. However, previous studies on GR [97], $f(R)$ gravity [34, 98–99], and $f(R,T)$ gravity [100−104], as well as more recent studies on $f(R,\mathcal{L}_m,T)$ models [32, 105], have shown that matter–geometry couplings significantly shift M–R relations. The compactness and redshift trends obtained are qualitatively consistent with these results. Our approach differs by employing the generalized $f(R,\mathcal{L}_m,T)$ framework together with the MGD technique.

Unraveling the true mass and radius of pulsars remains a central challenge in compact star astrophysics. Despite notable observational progress, these parameters still involve uncertainties owing to extreme physical conditions and complex matter interactions inside such objects. In this study, we propose a refined modeling strategy within the extended $f(R,\mathcal{L}_m,T)$ gravity framework to better capture the structure of pulsars under modified gravitational dynamics. To connect our theoretical model with observational reality, we compared it to reliable data from well-studied pulsars, including Her X-1 [69], LMC X-4 [70], Cen X-3 [71], 4U 1538-52 [72], Vela X-1 , PSR J1614-2230 [73], and PSR J0740+6620 [74]. These compact objects span a wide mass range and provide a robust testing ground for assessing the predictive power and flexibility of the proposed model.

In future work, we plan to extend this analysis by numerically constructing explicit M–R sequences in $f(R,\mathcal{L}_m,T)$ gravity and comparing them directly to GR, $f(R)$, and $f(R,T)$ predictions, thereby offering deeper insights into the physics of ultra-dense stars.

V. CONCLUSION

In this research, we employed the MGD approach for gravitational decoupling within the framework of $f(\mathcal{R},\mathcal{L}_m,T)$ gravity to construct anisotropic compact star models based on a class-1 embedding spacetime. In the literature, this method has proven to be highly effective for developing interior solutions of self-gravitating systems, enabling the investigation of gravitational effects from various perspectives within spherically symmetric configurations. In the present study, we have utilized Ovalle's gravitational decoupling technique [92] along with the MGD approach in the context of $f(\mathcal{R},\mathcal{L}_m,T)$ gravity to formulate physically viable models of compact stellar objects with anisotropic pressure. Within this framework, one of the metric potentials is deformed by introducing an additional gravitational source that decouples the original field equations into two separate systems. The first system corresponds to the standard perfect fluid Einstein equations described by $T_{\mu\nu}$, whereas the second governs the anisotropic source $\vartheta_{\mu\nu}$, forming a quasi-Einstein system. Notably, these two sources interact solely through gravitational interaction, without any direct energy exchange. We introduced deformation by modifying the radial component of the metric through an appropriate choice of the function $\psi(r)$ [64–65], ensuring regularity in the metric functions and all essential physical parameters throughout the stellar interior. It is important to note that setting the coupling parameter $\beta=0$ recovers the original field equations of the theory. Additionally, constants $\mathbb{A}$, $\mathbb{B}$, and c were determined by matching the interior solution to the exterior Schwarzschild geometry.

The effective radial pressure, $p_r^{\text{eff}}=0$, at the boundary, derived from the second fundamental form of the junction conditions, incorporates both the isotropic pressure p_r and deformation function $\psi(r)$, which arises because of the additional source $\tilde{\theta}_{\mu\nu}$. Using realistic observational data, we determined the constants A, B, and c for seven compact stellar candidates: Her X-1, Cen X-3, LMC X-4, Vela X-1, PSR J1614-2230, 4U 1608-52, and PSR

J0740+6620. The corresponding results are presented in Tables 1 and 2. The compact star Cen X-3 was selected for graphical examination because its radius ($\mathcal{R} = 9.178$) lies in an optimal range that allows a comprehensive illustration of all physical parameters, including energy density, pressure profiles, anisotropy, energy conditions, and equilibrium forces. Larger radii were required to exhibit the full behavior of these quantities, making Cen X-3 a suitable candidate. For graphical analysis, we evaluated the physical behavior of the model under two distinct scenarios: one involving variations in the coupling parameter β, and the other involving changes in the deformation parameter n, both using Cen X-3 as the reference model. We summarize the key conclusions derived from this study as follows:

- Figures 1(a) and 1(b) show how gravitational decoupling affects the metric potentials for both scenarios when using Cen X-3 star's observational data and constants $A = -0.0403881$, $B = -0.0306402$, and $C = 0.00454612$. The metric potentials clearly indicate positive and monotonically decreasing behavior within the star before diminishing at the boundary, fostering our model's regularity and stability.

- Figures 2(a), 2(b), 2(c), and 3(a) show positive, non-singular, and monotonically decreasing behaviors of energy density and pressure inside the stellar structure. It was noticed that the radial pressure vanished at the star's surface, validating the model's physical consistency.

- Figures 4(c) and 5(c) depict the trend of the anisotropy profile, which is a positive increasing function of r and is zero at the boundary (indicating that the radial and tangential pressures are equal).

- Figures 3(b) and 3(c) illustrate the negative and monotonically declining gradients of the energy density and pressures, which satisfy the required constraint of vanishing at $r = 0$ given in Eq. (50), and hence assured the model's physical validity.

- Furthermore, Figs. 4(a), 4(b), 5(a), and 5(b) show the energy condition inequalities, which demonstrate that all energy bounds (NEC, SEC, DEC, and WEC) have been validated throughout the stellar interior given in Eq. (51).

- Figure 6 depicts the hydrostatic equilibrium of the model given by Eq. (52), which is derived from balancing the hydrostatic force (F_h), gravitational force (F_g), anisotropic force (F_a), and modified force (F_m) due to $f(\mathcal{R}, \mathcal{L}_m, T)$ gravity. This ensures that the forces counterbalance each other, preventing gravitational collapse and confirming the stability of the model.

- The EoS, as shown in Figs. 7(a) and 7(b), indicates that all values are between 0 and 1.

- Additionally, the speeds of sound (v_r^2 & v_t^2) remained lower than the speed of light throughout the stellar interface, as shown in Figs. 8 and 9(a). This clearly satisfies the criteria for causality and stability.

- Furthermore, the adiabatic index surpasses the essential value of 4/3, thereby guaranteeing static stability. Furthermore, Herrera's cracking conditions were satisfied.

Clearly, the TOV equation holds true in the re-designed framework, indicating that our solutions reflect physically viable, stable, and equilibrium compact star models. Tables 3 and 4 show the mass, redshift, and compactness values, with and without MGD. Notably, we observed that negative values of the coupling parameter β allow for greater mass packing, as evidenced by the increased values of mass, redshift, and compactness compared with that of the un-deformed case. Figure 10 clearly demonstrates that these values increase monotonically with r, reaching the highest value at the surface of the star for $\beta = -0.5$. Figure 11 shows the effect of varying n with these parameters, with the maximum values occurring at $n = 3$ for $\beta = -0.2$.

This study concludes by highlighting the important effects of gravitational decoupling via the MGD technique on the compactness ($u = M/\mathcal{R}$) and total mass of the compact star models. When β assumes negative values, the additional gravitational source, induced and governed by the coupling parameter β, enables a higher mass confinement within the stellar structure. This realization underscores the flexibility and strength of the MGD approach for constructing stable and physically consistent compact star solutions with anisotropic pressures and extended gravitational influences.

In particular, our findings differ from those of previous studies in other modified gravity models, as shown in Table 5, where such significant variation in mass due to deformation and coupling has not been reported within the context of $f(\mathcal{R}, \mathcal{L}_m, T)$ gravity. Specifically, the simultaneous increase and decrease in mass and compactness with different β values is a novel result of this theory, revealing new physical insights that have not been previously explored. Table 5 presents a comparative summary of our model with other recent studies, clearly emphasizing the theoretical and physical advancements achieved. In $f(R)$ theory, Sharif and Aslam [106] explored anisotropic spherical symmetric solutions through an extended gravitational decoupling approach. Two types of solutions were presented by considering the Starobinsky model of $f(R)$ gravity along with the Krori-Barua metric potential. It was shown that one of the two developed mod-

els exhibited locally unstable conduct when different coupling parameter values were used. In another study [58], the authors investigated the construction of anisotropic static spheres by using the metric potentials of the Tolman V solution and MGD scheme in $f(R,T^2)$ gravity. Solutions were obtained by imposing three different constraints, and the first two models were physically viable and stable only when small choices of decoupling parameters were considered. In the present study, we considered the linear $f(R,L_m,T)$ models and found that for all choices of parameter β, the obtained model exhibited stable and physically valid behavior. In a recent study, Singh *et al.* [65] explored anisotropic compact star configurations for a self-gravitating structure using a MGD scheme, along with embedding class-1 spacetime in the GR framework. They performed a graphical analysis by considering different variations of the coupling parameters α and n. It is shown that all the physical characteristics are satisfied when positive values of α are considered. Our study extends this work by involving curvature-matter coupling and the results obtained are quite similar. Using the same metric potential with the gravitational coupling approach, Hira *et al*. [64] modeled compact stellar structures using Rastall theory. Using different measures of graphical analysis, physically valid models were obtained when positive coupling parameter values were assumed, and our results were also in agreement with their findings.

The effective implementation of this technique within the framework of $f(\mathcal{R},\mathcal{L}_m,T)$ gravity offers promising new directions for the study of compact stars in alternative gravity theories and enhances our understanding of the internal composition and evolution of dense astrophysical objects.

References

[1] J. M. Lattimer and M. Prakash, Phys. Rev. Lett. **94**, 111101 (2005)
[2] B. P. Abbott, R. Abbott, T. D. Abbott *et al*., Phys. Rev. Lett. **119**, 161101 (2017)
[3] K. Akiyama, A. Alberdi, W. Alef *et al*., Astrophys. J. Lett. **875**, L1 (2019)
[4] S. Perlmutter, G. Aldering, G. Goldhaber *et al*., Astrophys. J. **517**, 565 (1999)
[5] A. G. Riess, A. V. Filippenko, P. Challis *et al*., Astron. J. **116**, 1009 (1998)
[6] D. N. Spergel, L. Verde, H. V. Peiris *et al*., Astrophys. J. Suppl. Ser. **148**, 175 (2003)
[7] E. Komatsu, J. Dunkley, M. R. Nolta *et al*., Astrophys. J. Suppl. Ser. **180**, 330 (2009)
[8] S. W. Hawking and R. Laflamme, Phys. Lett. B **209**, 39 (1988)
[9] A. Narimani, N. Afshordi, and D. Scott, J. Cosmo. Astropart. Phys. **08**, 049 (2014)
[10] J. S. Farnes, Astron. Astrophys. **620**, A92 (2018)
[11] T. P. Sotiriou and V. Faraoni, Rev. Mod. Phys. **82**, 451 (2010)
[12] S. Capozziello and M. De Laurentis, Phys. Rep. **509**, 167 (2011)
[13] K. Hayashi and T. Shirafuji, Phys. Rev. D **19**, 3524 (1979)
[14] E. E. Flanagan and E. Rosenthal, Phys. Rev. D **75**, 124016 (2007)
[15] J. B. Dent, S. Dutta, and E. N. Saridakis, J. Cosmol. Astropart. Phys. **2011**, 009 (2011)
[16] K. Bamba, C. Q. Geng, C. C Lee *et al*., J. Cosmo. Astropart. Phys. **2011**, 021 (2011)
[17] M. Zubair, F. Kousar, and R. Saleem, Chin. J. Phys. **65**, 355 (2020)
[18] F. Kousar, R. Saleem, and M. Zubair, Adv. High Energy Phys. **2018**, 3085761 (2018)
[19] M. Zubair, F. Kousar, and S. Waheed, Can. J. Phys. **97**(8), 880 (2019)
[20] N. Montelongo Garcia, F. S. N. Lobo, J. P. Mimoso *et al*., J. Phys. Conf. Ser. **314**, 012056 (2011)
[21] S. K. Maurya, A. Errehymy, D. Deb *et al*., Phys. Rev. D **100**, 044014 (2019)
[22] M. Caruana, G. Farrugia, and J. L. Said, Eur. Phys. J. C **80**, 640 (2020)
[23] E. Gudekli, M. Zubair, M. J. Kamran *et al*., Int. J. Geom. Meth. Mod. Phys. **19**(4), 2250056 (2022)
[24] R. Saleem, M. I. Aslam, and M. Zubair, Eur. Phys. J. Plus **136**(10), 1078 (2021)
[25] M. Zubair, A. Ditta, S. Waheed *et al*., Chin. J. Phys. **77**, 1827 (2022)
[26] S. K. Maurya, J. Kumar, and S. Kiroriwal, JHEAP **44**, 194 (2024)
[27] S. K. Maurya, A. Errehymy, Y. Saginayev *et al*., Phys. Dark Univ. **49**, 101977 (2025)
[28] S. K. Maurya, K. N. Singh, M. Govender *et al*., Astrophys. J. Suppl. **269**(2), 35 (2023)
[29] L. V. Jaybhaye, R. Solanki, S. Mandal *et al*., Phys. Lett. B **831**, 137148 (2022)
[30] Z. Haghani and T. Harko, Eur. Phys. J. C **81**, 615 (2021)
[31] M. Zubair, S. Waheed, Q. Muneer *et al*., Fortsch. Phys. **71**(8), 2300018 (2023)
[32] C. E. Mota, J. M. Z. Pretel, C. O. V. Flores *et al*., Eur. Phys. J. C **84**, 673 (2024)
[33] G. G. L. Nashed and W. El Hanafy, J. Cosmo. Astropart. Phys. **09**, 038 (2023)
[34] G. G. L. Nashed and S. Capozziello, Eur. Phys. J. C **84**, 521 (2024)
[35] G. G. L. Nashed, Astrophys. J. **950**(2), 129 (2023)
[36] A. Das, F. Rahaman, B. K. Guha *et al*., Eur. Phys. J. C **76**, 654 (2016)
[37] J. Kumar, H. D. Singh, and A. K. Prasad, Phys. Dark Univ. **34**, 100880 (2021)
[38] A. K. Yadav, M. Mondal, and F. Rahaman, Pramana J. Phys. **94**, 90 (2020)
[39] D. Taser and S. S. Dogru, Astrophys. Space Sci. **368**(6), 49 (2023)
[40] J. Ovalle, R. Casadio, R. da Rocha *et al*., Eur. Phys. J. C **78**, 122 (2018)
[41] L. Randall and R. Sundrum, Phys. Rev. Lett. **83**, 4690 (1999)
[42] R. Casadio, J. Ovalle, and R. da Rocha, Class. Quantum

Gravit. **32**, 215020 (2015)
[43] J. Ovalle, Int. J. Mod. Phys. D **18**, 837 (2009)
[44] R. Casadio and J. Ovalle, Phys. Lett. B **715**, 251 (2012)
[45] J. Ovalle, Phys. Lett. B **788**, 213 (2019)
[46] R. da Rocha, Eur. Phys. J. C **77**, 355 (2017)
[47] R. Casadio, P. Nicolini, and R. da Rocha, Class. Quantum Gravit. **35**, 185001 (2018)
[48] C. L. Heras and P. Leon, Fortsch. Phys. **66**, 1800036 (2018)
[49] M. Estrada, F. Tello-Ortiz, Eur. Phys. J. Plus **133**, 453 (2018)
[50] M. Sharif and S. Saba, Eur. Phys. J. C **78**, 921 (2018)
[51] E. Morales and F. Tello-Ortiz, Eur. Phys. J. C **78**, 618 (2018)
[52] M. Estrada and R. Prado, Eur. Phys. J. Plus **134**, 168 (2019)
[53] E. Contreras and P. Bargueno, Eur. Phys. J. C **78**, 558 (2018)
[54] H. Azmat and M. Zubair, Phys. Dark Univ. **37**, 101049 (2022)
[55] H. Azmat, R. Khalid, M. Zubair *et al*., Commun. Theor. Phys. **77**(6), 065401 (2025)
[56] H. Azmat, F. Tello-Ortiz, M. Zubair *et al*., Phys. Scripta **98**(1), 015010 (2022)
[57] S. K. Maurya, F. Tello-Ortiz, Phys. Dark Univ. **27**, 100442 (2020)
[58] M. Sharif and S. Iltaf, Physica Scripta **97**, 075002 (2022)
[59] S. K. Maurya, A. Errehymy, B. Dayanandan *et al*., JHEAP **45**, 46 (2025)
[60] S. K. Maurya, A. Errehymy, K. N. Singh *et al*., J. Cosmol. Astropart. Phys. **04**, 004 (2025)
[61] H. Azmat and M. Zubair, Eur. Phys. J. Plus **136**(1), 112 (2021)
[62] S. Sahlu, A. H. A. Alfedeel, and A. Abebe, Eur. Phys. J. C **84**(9), 982 (2024)
[63] K. Lake, Phys. Rev. D **67**, 104015 (2003)
[64] H. Sohail, A. Ditta, I. Mahmood *et al*., Eur. Phys. J. Plus **139**(8), 695 (2024)
[65] K. N. Singh, S. K. Maurya, M. K. Jasim *et al*., Eur. Phys. J. C **79**(10), 851 (2019)
[66] D. M. Pandya, B. Thakore, R. B. Goti *et al*., Astrophys. Space Sci. **365**(2), 30 (2020)
[67] S. N. Pandey and S. P. Sharma, Gen. Relativ. Gravit. **14**, 113 (1982)
[68] E. Morales and F. Tello-Ortiz, Eur. Phys. J. C **78**, 841 (2018)
[69] M. K. Abubekerov, E. A. Antokhina, A. M. Cherepashchuk *et al*., Astron. Rep. **52**, 379 (2008)
[70] M. L. Rawls, J. A. Orosz, J. E. McClintock *et al*., Astrophys. J. **730**, 25 (2011)
[71] S. Naik, B. Paul, and Z. Ali, Astrophys. J. **737**, 79 (2011)
[72] F. E. Marshall, L. Angelini, IAU Circ. **6331**, 1 (1996)
[73] Z. Arzoumanian *et al*. (NANOGrav Collaboration), Astrophys. J. Suppl. **235**(2), 37 (2018)
[74] M. Miller, F. K. Lamb, A. Dittmann *et al*., APJL **887**, L24 (2019)
[75] A. Chanda, S. Dey, and B. C. Paul, Eur. Phys. J. C **79**, 502 (2019)
[76] B. V. Ivanov, Phys. Rev. D **65**, 104001 (2002)
[77] S. W. Hawking and G. F. R. Ellis, *The Large Scale Structure of Space-Time*, (Cambridge: Cambridge University Press, 2023).
[78] R. Bousso, Rev. Mod. Phys. **74**, 825 (2002)
[79] S. Das, F. Rahaman, and L. Baskey, Eur. Phys. J. C **79**, 853 (2019)
[80] A. Di Prisco, L. Herrera, and V. Varela, Gen. Relativ. Gravit. **29**, 1239 (1997)
[81] L. Herrera, Phys. Lett. A **165**, 206 (1992)
[82] H. Abreu, H. Hernandez, and L. A. Nunez, Classic. Quantum Gravit. **24**, 4631 (2007)
[83] H. Andreasson, Commun. Math Phys. **288**, 715 (2009)
[84] S. Chandrasekhar, Astrophys. J. **140**, 417 (1964)
[85] D. D. Doneva and S. S. Yazadjiev, Phys. Rev. D **85**, 124023 (2012)
[86] H. O. Silva, C. F. B. Macedo, E. Berti *et al*., Class. Quantum Gravit. **32**, 145008 (2015)
[87] C. C. Moustakidis, Gen. Relativ. Gravit. **49**, 68 (2017)
[88] M. K. Mak and T. Harko, Proc. R. Soc. London Ser. A Math Phys. Eng. Sci. **459**, 393 (2003)
[89] C. G. Bohmer and T. Harko, Class. Quantum Gravit. **23**, 6479 (2006)
[90] C. Arias, F. Tello-Ortiz, and E. Contreras, Eur. Phys. J. C **80**, 463 (2020)
[91] S. Chakraborty, S. SenGupta, J. Cosmo. Astropart. Phys. **05**, 032 (2018)
[92] F. Tello-Ortiz, Eur. Phys. J. C **80**, 413 (2020)
[93] H. A. Buchdahl, Phys. Rev. **116**, 1027 (1959)
[94] M. F. Shamir, Z. Asghar, and A. Malik, Fortsch. Phys. **70**, 12 (2022)
[95] G. Abbas, A. Kanwal, and M. Zubair, Astrophys. Space Sci. **357**(2), 109 (2015)
[96] T. Tangphati, I. Sakalli, A. Banerjee *et al*., Chin. Phys. C **49**(2), 025110 (2025)
[97] S. K. Maurya, M. K. Jasim, A. Errehymy *et al*., Eur. Phys. J. C **85**(3), 321 (2025)
[98] R. Kumar, S. K. Maurya, Y. Sekhmani *et al*., Nucl. Phys. B **1018**, 116984 (2025)
[99] M. Zubair and G. Abbas, Astrophys. Space Sci. **361**, 342 (2016)
[100] A. Errehymy, Y. Khedif, G. Mustafa *et al*., Chin. J. Phys. **77**, 1502 (2022)
[101] P. H. R. S. Moraes, J. D. V. Arbañil, and M. Malheiro, JCAP **06**, 005 (2016)
[102] K. N. Singh, S. K. Maurya, A. Errehymy *et al*., Phys. Dark Univ. **30**, 100620 (2020)
[103] K. N. Singh, A. Errehymy, F. Rahaman *et al*., Chin. Phys. C **44**(10), 105106 (2020)
[104] M. Rahaman, K. N. Singh, A. Errehymy *et al*., Eur. Phys. J. C **80**(3), 272 (2020)
[105] J. A. S. Fortunato, P. H. R. S. Moraes, E. Brito *et al*., Phys. Dark Univ. **48**, 101893 (2025)
[106] M. Sharif and M. Aslam, Eur. Phys. J. C **81**, 641 (2021)